Article

Cell Chemical Biology

Small-molecule inhibitors of the protein kinase DYRK as potential therapeutic candidates in cancer

Graphical abstract

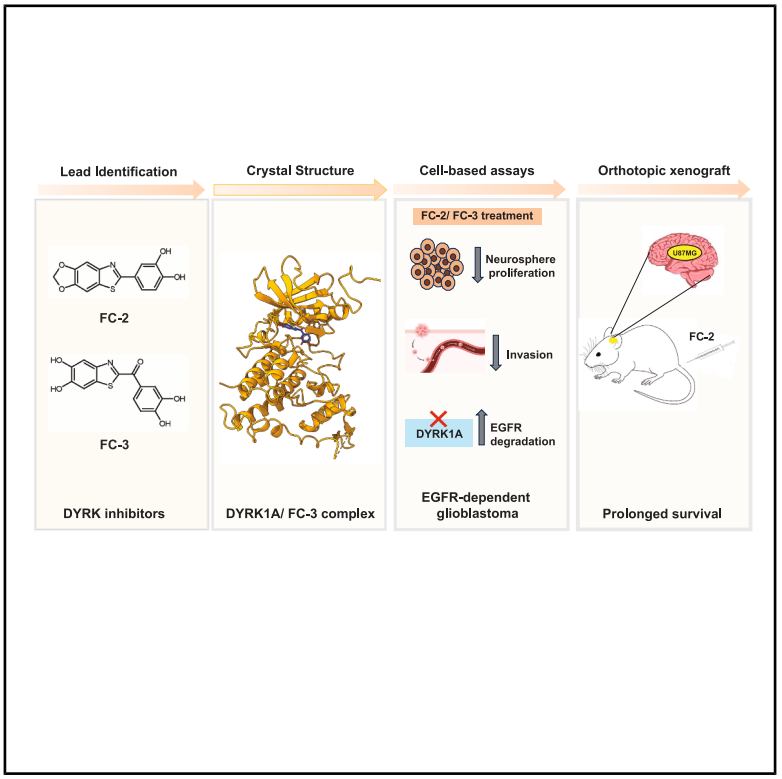

Authors

Prabhadevi Venkataramani, Elad Elkayam, Ankur Garg, ..., Leemor Joshua-Tor, Yousef Al-Abed, Nicholas K. Tonks

Correspondence

tonks@cshl.edu

In brief

Venkataramani et al. identify two potent, ATP-competitive inhibitors of DYRK1A, FC-2 and FC-3, which suppress EGFR-driven glioblastoma (GBM) growth. Inhibitor-resistant mutants confirm DYRK1A as the functional target, highlighting FC-2 and FC-3 as promising therapeutic candidates in EGFR-dependent GBM and other cancers.

Highlights

- FC-2 and FC-3 are potent, ATP-competitive, nanomolar inhibitors of DYRK1A
- Inhibitor-resistant DYRK1A mutants confirm on-target inhibition
- FC-2 and FC-3 reduce GBM neurosphere proliferation, invasion, and EGFR levels
- FC-2 crosses the blood-brain barrier and suppresses GBM tumor growth *in vivo*

Venkataramani et al., 2026, Cell Chemical Biology *33*, 810–822
June 18, 2026
https://doi.org/10.1016/j.chembiol.2026.05.005

CellPress

CellPress
OPEN ACCESS

Cell Chemical Biology

Article

Small-molecule inhibitors of the protein kinase DYRK as potential therapeutic candidates in cancer

Prabhadevi Venkataramani,[1] Elad Elkayam,[1,3,4] Ankur Garg,[1,3] Kai Fan Cheng,[2] Ahmad Altiti,[2] Mingzhu He,[2] Khushabu Thakur,[2] Evdokia Michalopoulou,[1] Camila Gonzalez,[1] Christy Felice,[1] Linda Van Aelst,[1] Darryl Pappin,[1] Leemor Joshua-Tor,[1,3] Yousef Al-Abed,[2] and Nicholas K. Tonks[1,5,*]

[1]Cold Spring Harbor Laboratory, 1 Bungtown Road, Cold Spring Harbor, NY 11724, USA
[2]Feinstein Institutes for Medical Research, Manhasset, NY 11030, USA
[3]Howard Hughes Medical Institute, Cold Spring Harbor Laboratory, Cold Spring Harbor, NY 11724, USA
[4]Present address: Ventus Therapeutics, Waltham, MA 02453, USA
[5]Lead contact
*Correspondence: tonks@cshl.edu
https://doi.org/10.1016/j.chembiol.2026.05.005

SIGNIFICANCE DYRK1A has emerged as a critical regulator of oncogenic signaling, functioning to stabilize receptor tyrosine kinases such as EGFR through phosphorylation of substrates including Sprouty2. Despite this central role, the mechanisms by which DYRK1A sustains growth-promoting signaling and its tractability as a therapeutic target remain incompletely defined. Here, we identify and characterize two benzothiazole-derived small-molecule inhibitors, FC-2 and FC-3, as potent and reversible inhibitors of DYRK1A. Using structural, biochemical, and cell-based approaches, we demonstrate that these compounds directly engage DYRK1A in an ATP-competitive manner, with specificity confirmed through inhibitor-resistant gatekeeper mutants. Mechanistically, our studies define a DYRK1A-Sprouty2 signaling axis in which phosphorylation of Sprouty2 at Thr75 regulates EGFR stability and downstream signaling. Pharmacological inhibition of DYRK1A with FC-2 and FC-3 phenocopies genetic loss of DYRK1A, leading to impaired receptor stability and attenuation of oncogenic signaling outputs. Glioblastoma (GBM) remains one of the most aggressive and lethal primary brain tumors, with limited treatment options and poor patient survival. In EGFR-dependent GBM models, DYRK1A inhibition disrupts neurosphere self-renewal, invasion, and tumor growth, establishing GBM as a disease context in which this signaling dependency is functionally relevant. Notably, our DYRK inhibitor FC-2 penetrates the blood-brain barrier and suppresses tumor growth in both subcutaneous and intracranial xenograft models, supporting the translational potential of targeting DYRK1A in the central nervous system. Collectively, these findings position DYRK1A as a key signaling node that integrates kinase-driven oncogenic pathways and establish selective small-molecule inhibitors as powerful tools to interrogate its function. More broadly, this work provides a conceptual and therapeutic framework for targeting DYRK1A across cancers characterized by aberrant receptor tyrosine kinase signaling.

SUMMARY

Dual-specificity tyrosine-regulated kinase 1A (DYRK1A) is crucial for normal brain development, and its disruption is linked to various cancers. DYRK1A drives glioblastoma (GBM) progression via stabilization of epidermal growth factor receptor (EGFR). Here, we describe two benzothiazole-derived DYRK inhibitors, FC-2 and FC-3, obtained by structure-activity optimization of a natural product lead. Both compounds inhibited DYRK1A with nanomolar potency and displayed selectivity across a kinase panel. The co-crystal structure of FC-3 with DYRK1A revealed ATP-competitive binding, with interactions at the hinge region. The DYRK-specific phenylalanine gatekeeper residue contributed to target selectivity. Generation of inhibitor-resistant mutants confirmed DYRK1A as the primary cellular target. In GBM cell-based models, FC-2 and FC-3 impaired neurosphere self-renewal, cell invasion, and EGFR stability, phenocopying DYRK1A loss. FC-2 crossed the blood-brain barrier and suppressed tumor growth, prolonging survival in intracranial xenografts. These findings identify FC-2 and FC-3 as small-molecule nanomolar inhibitors of DYRK1A, with potential therapeutic utility in GBM.

INTRODUCTION

Dual-specificity tyrosine-regulated kinases (DYRKs) are conserved kinases belonging to the CMGC (including cyclin-dependent kinases [CDKs], mitogen-activated protein kinases [MAP kinases], glycogen synthase kinases [GSKs], and CDK-like kinases) family[1]; they phosphorylate substrates at serine and threonine residues while being activated by autophosphorylation of a single tyrosine residue on their activation loop during translation.[2] There are five known DYRK isoforms: DYRK1A, DYRK1B, DYRK2, DYRK3, and DYRK4.[3] Among all DYRK isoforms, DYRK1A is the best characterized and the most extensively studied. It is localized in the Down syndrome's critical region of chromosome 21, which makes it a strong candidate gene for learning defects associated with trisomy 21 or Down syndrome. Children with Down syndrome have an increased risk of developing acute lymphoblastic leukemia (ALL) and acute megakaryoblastic leukemia (AMKL).[4,5] In Alzheimer disease, DYRK1A overexpression enhances the levels of Tau proteins, contributing to neurodegeneration.[6] DYRK1A has also been reported to inhibit microtubule assembly by mediating Tau hyperphosphorylation at several residues.[7,8] DYRK1A also inhibits the splicing factor 9G8 (SRSF7) leading to amyloid precursor protein (APP) cleavage, potentially contributing to Aβ production *in vivo*[9]. In addition to cognitive impairment, DYRK1A hyperactivity has also been correlated with diabetes and other cancers.[10,11] DYRK1A upregulation has also been linked to various cancer types, including glioblastoma (GBM),[12] lung cancer,[13,14] head and neck squamous cell carcinoma (HNSCC),[15] as well as pancreatic adenocarcinoma (PDAC).[16] DYRK1A has been implicated in GBM tumorigenesis as it potentiates EGFR signaling by preventing endocytic degradation of the receptor.[17,18] Given its diverse roles across various diseases, including cancer, pharmacological inhibition of DYRK1A has emerged as a promising therapeutic strategy for a variety of major indications.

Recent advances in DYRK inhibitor development reflect growing recognition of DYRK1A's role in diverse diseases. Current inhibitors include natural and synthetic compounds such as harmine,[19] epigallocatechin gallate (EGCG),[20] and benzothiazole derivatives including INDY,[21] D-luciferin,[22,23] and PST-001.[24] Multiple studies have also employed a 6-hydroxybenzothiazol-2-yl urea scaffold to improve the potency and selectivity of DYRK1A inhibitors.[25–27] Notable benzothiazole-based compounds from this work include b24, b27, b1, and b20. Among these, b1 and b20 were shown to reduce α-synuclein oligomer aggregation, whereas b27 inhibited F3B1 phosphorylation in HeLa cells in addition to targeting DYRK1A.[27] Recently, there has been exciting development of the dual DYRK/CLK inhibitor leucettinib 21 (LCTB-21), which has entered phase 1 clinical testing as a potential therapeutic target for Alzheimer disease and Down syndrome.[28–32] Nevertheless, several DYRK inhibitors have faced challenges, including side effects and lack of selectivity, in their development. For example, in addition to DYRK, harmine is a potent monoamine oxidase (MAO)-A inhibitor that leads to hallucinogenic and toxic side effects, which limit its therapeutic potential.[33] As such, this emphasizes the importance of identifying DYRK1A inhibitors.

In a previous study from our lab, we have reported the isolation of a fraction, A250, from fermented wheat germ extract (FWGE), using bioassay-guided fractionation.[34,35] To further our interest in the active components of FWGE, we purified and characterized CSH-4044, a small-molecule inhibitor that was tested against a panel of 140 kinases and displayed selectivity for the proviral integration site for Moloney murine leukemia virus (PIM) and DYRK families of kinase. We began a structure-activity relationship (SAR) optimization strategy to generate analogs of CSH-4044 that displayed improved selectivity toward either DYRK or PIM kinases. Following screening of 179 CSH-4044 analogs, we isolated two small-molecule inhibitors of DYRKs—FC-2 and FC-3—and validated them as potential therapeutic candidates for EGFR-dependent GBM, using different biochemical, cell-based, and *in vivo* studies.

RESULTS

FC-2 and FC-3 are nanomolar inhibitors of DYRKs

Our lab has previously reported the isolation of an active fraction of FWGE, A250, by bioassay-guided fractionation.[34] Since PIMs and DYRKs have been implicated in a wide variety of cancers and neurodegenerative and metabolic disorders,[36,37] inhibitors of these kinases may have broad therapeutic utility. Because CSH-4044 inhibits both DYRKs and PIMs, we were interested in optimizing selectivity toward either PIM or DYRK kinases. We completed a SAR optimization program, which yielded 179 analogs of CSH-4044 that we tested against both DYRK1A and PIM1 kinases, using a peptide-based *in vitro* kinase assay.[38] From the assay screen, we identified candidates that inhibited DYRK preferentially, inhibited PIM preferentially, or inhibited both. Of these, two candidates were synthesized with an HPLC purity of 95% or greater (Figures S1A and S1B; Table S1). Specificity of the isolated candidates was evaluated using a screen against a panel of 140 kinases at the International Center for Kinase Profiling (ICKP) at University of Dundee, UK (https://www.kinase-screen.mrc.ac.uk) (Figures 1A–1D; Table S2). Using *in vitro* kinase assays, we identified two nanomolar benzothiazole-derived compounds, FC-2 and FC-3, that inhibited the DYRK subfamily of kinases, with an IC_{50} of 19 and 53 nM, respectively (Figures 1E, 1F, and S5A).

Structural insights into the inhibition of DYRK1A by FC-3

We used an *in vitro* ATP-competitive assay to determine whether FC-2 and FC-3 bound to the ATP-binding pocket of DYRK1A. For this assay, we fixed different concentrations of FC-2 or FC-3 and the peptide substrate (KKISGRLSPIMTEQ) and varied ATP concentrations in a dose-dependent manner. Using the *in vitro* peptide-based kinase assay, we observed that the inhibition of DYRK1A by FC-2 and FC-3 could be overcame at higher concentrations of ATP, which suggested that both FC-2 and FC-3 were reversible, ATP-competitive inhibitors (Figures 2A and 2B).

We investigated the structural basis of FC-3-mediated DYRK1A inhibition by determining the crystal structure of the DYRK1A-FC-3 complex. DYRK1A-FC-3 crystals belonged to spatial group $P2_12_12_1$, with four complexes in the asymmetric unit. DYRK1A has a typical bilobed kinase fold, with the catalytic ATP-binding site nestled between the N and C lobes (Figure 2C). All four DYRK1A chains could be traced in the electron density map, except for amino acids 408–412, which stayed solvent

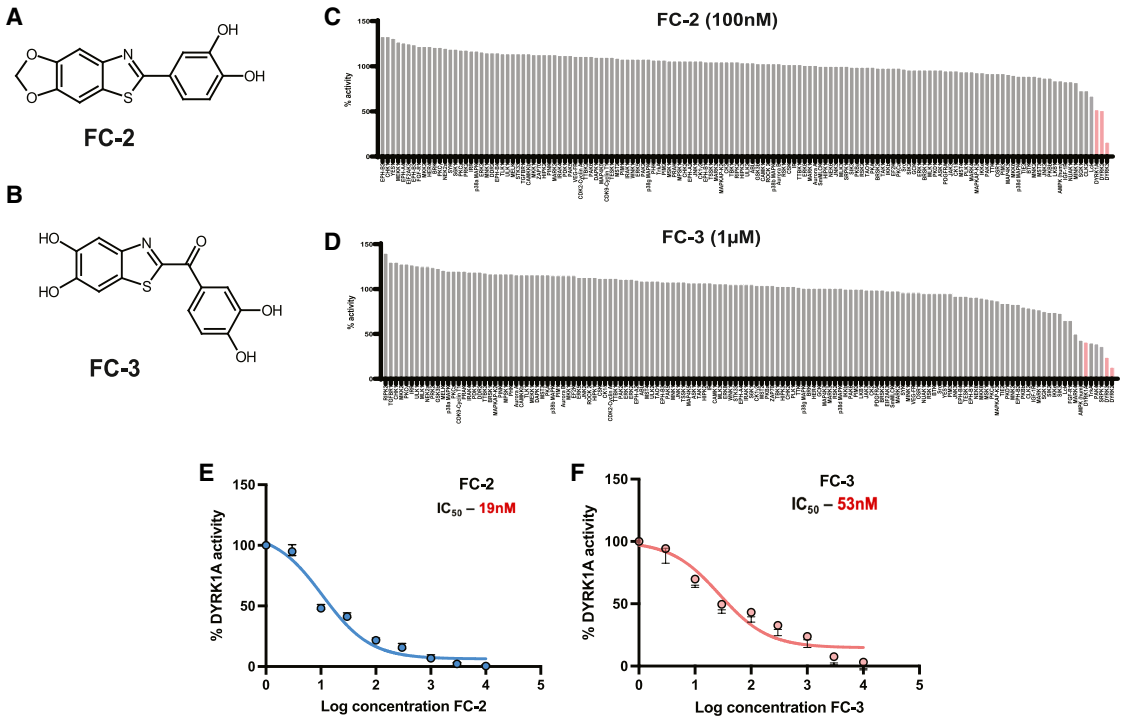

Figure 1. FC-2 and FC-3 are nanomolar inhibitors of DYRKs

(A and B) Chemical structures of (A) FC-2 and (B) FC-3.

(C and D) Evaluation of the specificity of (C) FC-2 (100 nM) and (D) FC-3 (1 μM), using a screen against a panel of 140 kinases (https://www.kinase-screen.mrc.ac.uk). The DYRK kinase family is marked in red.

(E and F) Determination of the IC_{50} values of (E) FC-2 (19 nM) and (F) FC-3 (53 nM) against DYRK1A, using an *in vitro* peptide-based kinase assay.

exposed. Clear electron density for the small molecule inhibitor FC-3 was observed between the N and C lobes, which allowed us to place the FC-3 molecule in the ATP-binding site in all four molecules in the asymmetric unit (Figures S2A–S2E). FC-3 assumes a planar geometry in the ATP-binding site and is stabilized via several hydrophobic interactions, H-bonds, and salt bridge interactions.

We found that FC-3 is surrounded by F238, V306, V222, L294, V173, L241, A186, and F170 side chains and is anchored via direct H-bonds with the main chain amide of L241 and the main chain carbonyl group of E239 (Figure 2D). The FC-3 carboxyl group in the central region interacts with conserved K188, while its dihydroxy benzene ring partially stacks on F170 and forms a H-bond with the main chain carbonyl group of K167 (Figure 2E). Most interactions between FC-3 and the kinase are conserved in the other molecules of the asymmetric unit, but a slightly different positioning of the dihydroxy benzene ring seems possible due to its rotation around the C–C bond that connects it with the FC-3 central carboxyl (Figure S2F).

Generation of inhibitor-resistant mutants of DYRK1A

One of the challenges in drug development is target selectivity. This selectivity problem is greater when targeting the active site of closely related subgroups of kinases that possess ATP-binding sites with a high sequence similarity.[39,40] It has been noted that the gold standard to evaluate drug selectivity is to identify a mutation or mutations in the target enzyme that can confer resistance to the inhibitor.[41] To understand the basis of selectivity toward DYRKs, we identified residues in the ATP-binding site of DYRK1A that might confer resistance to FC-2 and FC-3, using sequence alignment and crystal structure data (Figure 3A). The gatekeeper residue is located in the ATP-binding pocket near the hinge region connecting the N- and C-terminal lobes of the kinase and regulates the binding of small-molecule inhibitors or nucleotides to the kinase.[42–47] Interestingly, the gatekeeper residue for the DYRKs is a bulky phenylalanine, which is replaced by a smaller leucine for the PIMs.[48] Therefore, we generated point mutants of DYRK1A by substituting PIM residues into DYRK1A. Importantly, all the DYRK1A point mutants generated retained their kinase activity. Interestingly, the gatekeeper mutants F238L and M240R demonstrated resistance to FC-2 and FC-3 and showed higher IC_{50} values than DYRK1A wild type (Figures 3B and 3C). Additionally, a F238L-M240R double mutant displayed a further increase in IC_{50} values against both FC-2 and FC-3. In conclusion, this helped us identify the mutant forms of DYRK1A that retain their kinase activity but are resistant to FC-2 and FC-3 *in vitro*.

FC-2 and FC-3 reduce neurosphere proliferation and cell invasion by specifically targeting DYRK1A

Inhibition of DYRK1A has been shown to cause a decrease in the self-renewal capacity of GBM tumor-initiating cells (GBM-TICs).[17] Similarly, a reduction in neurospheres recovered from the subependymal zone (SEZ) was observed in DYRK1A heterozygous (*Dyrk1A*+/-) mouse brains.[49] Self-renewal refers to the

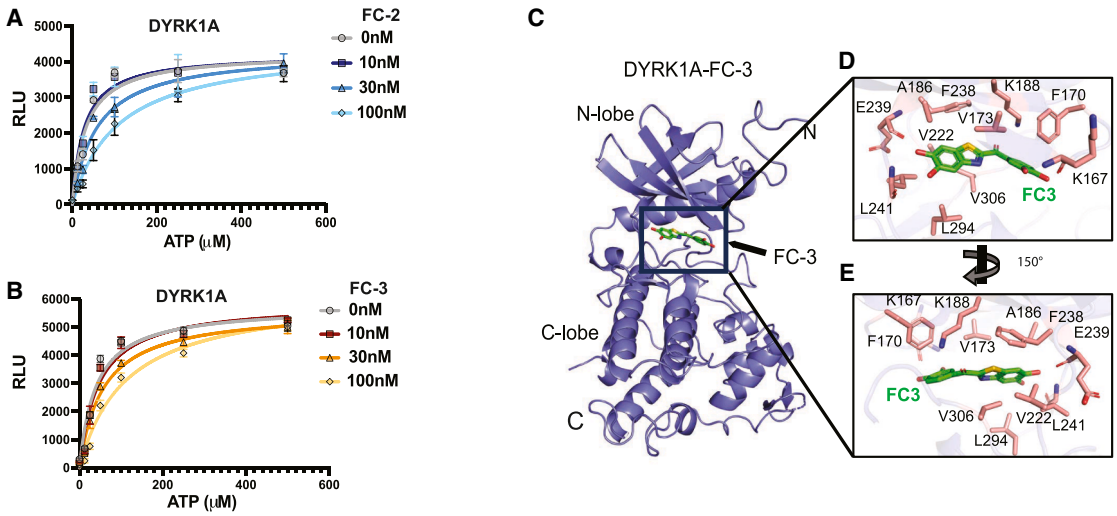

Figure 2. Structural insights into the inhibition of DYRK1A by FC-3

(A and B) *In vitro* ATP-competitive assays for the DYRK inhibitors (A) FC-2 and (B) FC-3, performed using increasing concentrations of ATP and the inhibitors against DYRK1A.

(C–E) A cartoon representation of the DYRK1A-FC-3 crystal structure; FC-3 (green sticks) binds in the ATP-binding site between the N and C lobes (C). A zoomed-in view of FC-3 interaction in the DYRK1A nucleotide-binding site in two views (D and E). Residues interacting with the inhibitor are shown in sticks.

ability of stem cells to divide and maintain their population.[50] To assess the effects of FC-2 and FC-3 on GBM self-renewal, we generated free-floating clusters of neural stem cells, called neurospheres, in the GBM cell line U87MG. Upon treatment with increasing concentrations of FC-2 and FC-3, we observed a dose-dependent decrease in neurosphere diameter as well as in the number of secondary spheres per well (Figures 4A and 4B). Similar effects were observed with the DYRK1A-knockout clones (Figure 4C). A comparable analysis was performed in a second GBM cell line, LN229, in which treatment with FC-2 or FC-3, as well as DYRK1A knockout, resulted in a dose-dependent reduction in neurosphere proliferation (Figures S3A–S3C) To test the engagement of DYRK1A as a target by FC-2 and FC-3, we rescued the DYRK1A-knockout clones with DYRK1A wild type and F238L-M240R double mutant, which retained its kinase activity but was resistant to FC-2 and FC-3 in our *in vitro* assays (Figure 4D). When we treated the rescued populations with FC-2 and FC-3, we noticed a decrease in neurosphere size and numbers only in the populations rescued by wild type but not in the F238L-M240R-mutant-expressing cells (Figures 4E and 4F). In addition, we generated DYRK2- and DYRK3-knockout clones (Figures S4A and S4B) and observed that they did not decrease neurosphere proliferation, unlike the DYRK1A-knockout clones (Figure S4C). These effects on neurosphere proliferation were additionally benchmarked against INDY, a DYRK inhibitor containing a benzothiazole scaffold (Figure S5B); FC-2 and FC-3 displayed greater efficacy than INDY in these neurosphere assays. These data support our *in vitro* results that DYRK1A is the key target of FC-2 and FC-3 in neurosphere assays.

In addition to playing a role in neurosphere self-renewal, DYRK1A also promotes GBM cell migration.[12] Using transwell

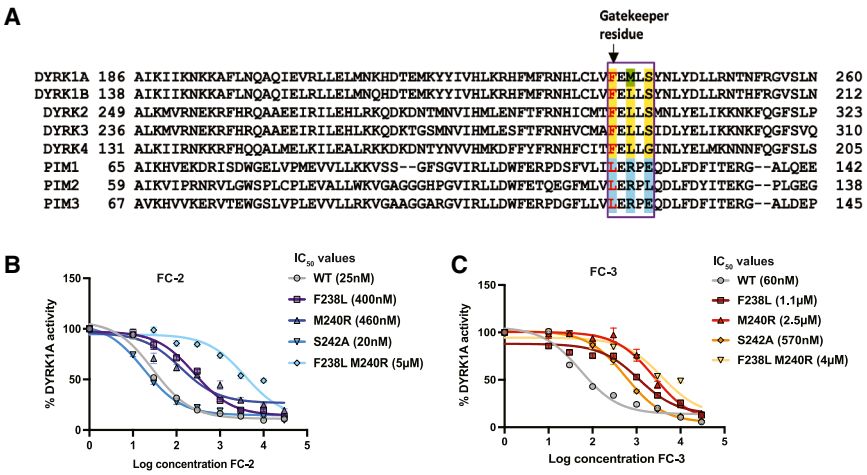

Figure 3. Generation of inhibitor-resistant mutants of DYRK1A

(A) Sequence alignment around the ATP-binding site of PIM and DYRK kinases; the residues that differ markedly in DYRKs compared to PIMs in the hinge region (purple boxed region) are shaded yellow (DYRKs) and cyan (PIMs). The gatekeeper residues of PIMs and DYRKs are marked in red. A distinct residue (Met240) of DYRK1A is shaded in green as it appears to be specific for the kinase.

(B and C) Determination of the IC_{50} values of the wild-type (WT) and mutant forms of DYRK1A (F238L, M240R, S242A, and F238L-M240R) against (B) FC-2 and (C) FC-3, using an *in vitro* peptide-based kinase assay; the mutant forms of DYRK1A retained their kinase activity.

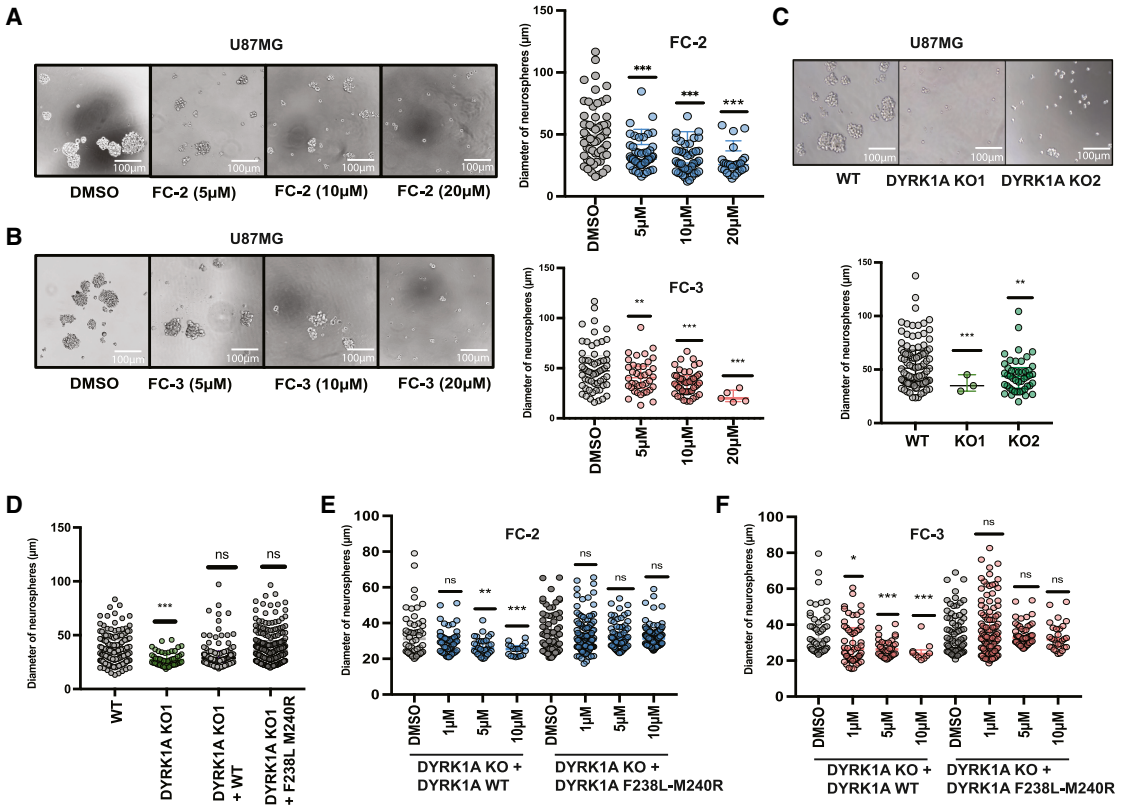

Figure 4. FC-2 and FC-3 decrease GBM neurosphere proliferation by targeting DYRK1A

(A and B) Left: representative images of U87MG wild-type (WT) neurospheres treated with DMSO or an increasing concentration of FC-2 and FC-3. Right: dot plots showing the quantification of the diameter and number of neurospheres; DMSO, FC-2, and FC-3 neurospheres are shown in gray, blue, and red respectively. Each dot represents a neurosphere.

(C) Top: representative images of U87MG WT and two clones of DYRK1A-knockout (KO1 and KO2) neurospheres. Bottom: dot plots showing the quantification of the diameter and number of U87MG WT (gray) and DYRK1A KO (green) neurospheres. Each dot represents a neurosphere.

(D) Dot plots showing the quantification of the diameter and number of neurospheres formed by U87MG WT (gray), DYRK1A KO (green), and the KO clones rescued with either WT (gray) or F238L-M240R double-mutant (dark gray) forms of DYRK1A. Each dot represents a neurosphere.

(E and F) Dot plots showing the quantification of the diameter and number of neurospheres of WT and DYRK1A KO clones rescued with either DYRK1A WT or DYRK1A F238L-M240R and treated with (E) FC-2 (blue) or (F) FC-3 (red). Each dot represents a neurosphere. Welch's *t* test (*$p < 0.05$; **$p < 0.005$; ***$p < 0.0005$).

assays, we observed that both FC-2 and FC-3 reduced the invasion of U87MG cells in a dose-dependent manner (Figure 5A). A comparable effect was also seen in the DYRK1A-knockout U87MG cell lines (Figure 5B). An independent study in the LN229 GBM cell line showed that the pharmacological inhibition with FC-2 or FC-3, as well as genetic ablation of DYRK1A, led to a dose-dependent suppression of invasion (Figures S3D and S3E). We also assessed the specificity of FC-2 and FC-3 in invasion, using rescue experiments with wild-type and mutant forms of DYRK1A (Figure 5C). Upon treatment with FC-2 and FC-3, we did not observe any significant reduction in the invasion ability of cells rescued with the DYRK1A F238L-M240R mutant as opposed to rescue with DYRK1A wild type (Figures 5D and 5E). The invasion phenotypes were also assessed against INDY, a DYRK inhibitor with a benzothiazole scaffold (Figure S5C); FC-2 and FC-3 displayed greater efficacy than INDY in these assays. Altogether, these data indicate that both FC-2 and FC-3 exert inhibitory effects on invasion through an on-target effect on DYRK1A in cell-based assays.

FC-2 and FC-3 destabilize EGFR in GBM cell-based models

It has been reported that DYRK1A inhibition leads to downregulation and endocytic degradation of the EGFR in GBM.[17,18] We evaluated the ability of FC-2 and FC-3 to downregulate EGFR levels and ERK phosphorylation, which is a marker of EGFR signaling. We observed a reduction in the total EGFR and ERK phosphorylation levels when the cells were treated with either FC-2 or FC-3 (Figures 6A and 6B). Moreover, a similar trend was noted in U87MG DYRK1A-knockout cell lines (Figure 6C). Using the LN229 cell line, we observed that both FC-2 and FC-3 treatments, as well as DYRK1A knockout, resulted in the downregulation of total EGFR levels (Figures S3F–S3H). In U87MG cells, we also detected the accumulation of EGFR upon DYRK1A inhibition or knockout when the cells were treated with either BaFA1, a lysosomal inhibitor, or MG132, a proteasomal inhibitor, indicating that EGFR was degraded endocytically upon FC-2 and FC-3 treatments (Figures 6D–6F). In addition, using an HA-tagged ubiquitin pulldown assay with U87MG-wild

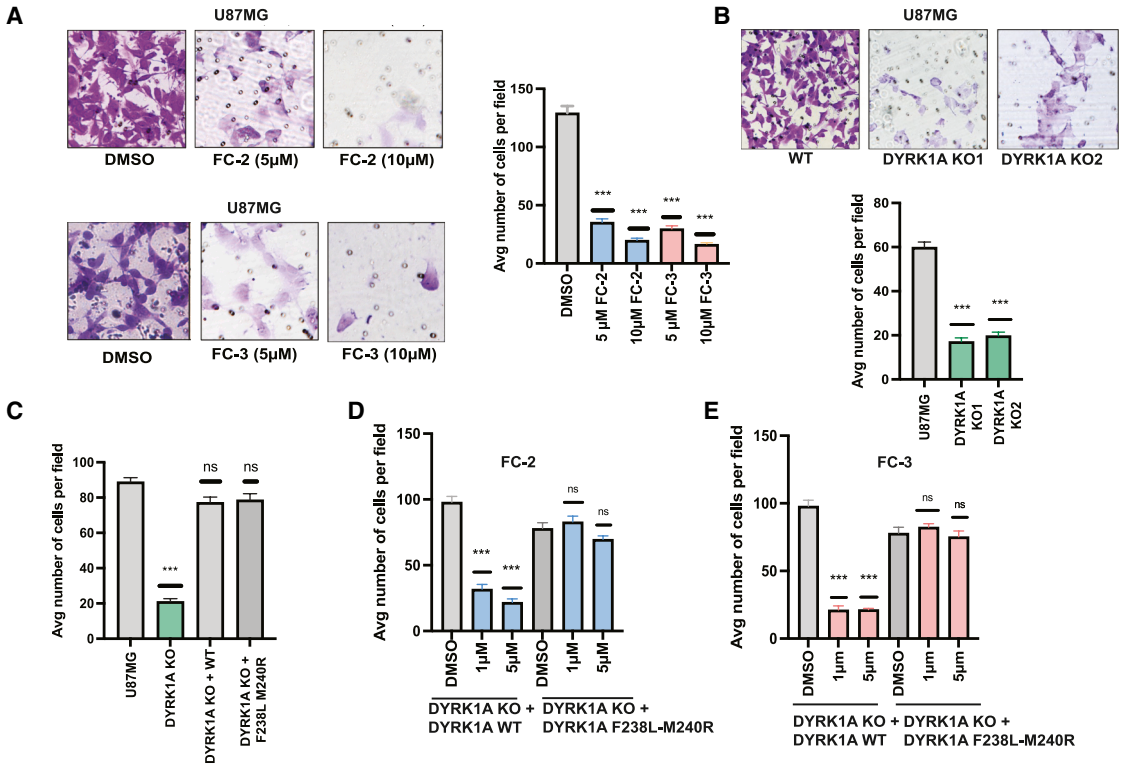

Figure 5. FC-2 and FC-3 reduce invasion by targeting DYRK1A

(A) Left: representative images of U87MG cells treated with FC-2 (left) and FC-3 (bottom) invasion stained with crystal violet. Right: quantification of the average number of cells per field that were able to cross the membrane in the invasion assay. Averages represent three independent trials in which 15–20 fields were counted.

(B) Top: representative images of U87MG wild-type (WT) and DYRK1A-knockout (KO) clones invasion stained with crystal violet. Right: quantification of the average number of cells per field that were able to cross the membrane in the invasion assay. Averages represent three independent trials in which 15–20 fields were counted.

(C) Right: quantification of the average number of cells per field that were able to cross the membrane in the invasion assay of U87MG WT (gray), DYRK1A-KO (green), and the KO clones rescued with either DYRK1A WT (gray) or DYRK1A F238L-M240R (dark gray). Averages represent three independent trials in which 15–20 fields were counted.

(D and E) Quantification of the average number of cells per field that were able to cross the membrane in the invasion assay of WT and DYRK1A-KO clones rescued with either DYRK1A WT or DYRK1A F238L-M240R and treated with (D) FC-2 (blue) or (E) FC-3 (red). Averages represent three independent trials in which 15–20 fields were counted. Bars represent the mean ± SEM; Welch's *t* test (*$p < 0.05$; **$p < 0.005$; ***$p < 0.0005$).

type and -knockout cells stably expressing ubiquitin, we observed an increased EGFR ubiquitination in case of FC-2- or FC-3-treated and DYRK1A-knockout cells relative to that in the non-treated or wild-type cells (Figures 6G and 6H). This indicates that FC-2 and FC-3 action enhanced EGFR ubiquitination, leading to its lysosomal degradation in EGFR-dependent GBM.

Previously, DYRK1A has been demonstrated to potentiate EGFR signaling by phosphorylating the MAP kinase modulator Sprouty2 (SPRY2) at Thr75.[17,18,49,51–53] We have demonstrated that the overexpression of SPRY2 in U87MG cells significantly attenuated the inhibitory effects of the DYRK inhibitors FC-2 and FC-3 on neurosphere proliferation, indicating that SPRY2 functions downstream of DYRK1A in promoting GBM cell growth (Figure S6A). Furthermore, knockout of SPRY2 phenocopied DYRK1A inhibition and knockout, showing reduced neurosphere proliferation and decreased total EGFR levels, which indicated that SPRY2 is a critical downstream effector of DYRK1A (Figures S6B and S6C). Mechanistically, re-expression of wild-type SPRY2 restored neurosphere proliferation, whereas the expression of a Thr75 phosphorylation-deficient SPRY2 mutant failed to rescue this phenotype (Figure S6D), which demonstrated that DYRK1A-mediated phosphorylation of SPRY2 at Thr75 is critical for SPRY2 function. Together, these results support a DYRK1A- SPRY2 signaling axis that sustains EGFR signaling in EGFR-dependent GBM.

FC-2 and FC-3 attenuate DYRK1A-mediated tumorigenesis in GBM animal models

We evaluated the effect of FC-2 and FC-3 in subcutaneous xenograft models. U87MG wild-type cells were injected into the flanks of Nu/J nude mice. Following daily administration of FC-2 and FC-3, we observed that the tumors in the FC-2 and FC-3 treatment cohorts were substantially smaller than those in the vehicle cohorts (Figures 7A and 7B). Moreover, the DYRK1A-knockout line cohort failed to develop any tumors (Figure 7C). Furthermore, we showed that the tumors in the treatment groups had markedly lower EGFR levels than those in the vehicle group (Figures 7D and 7E). This indicates that a possible

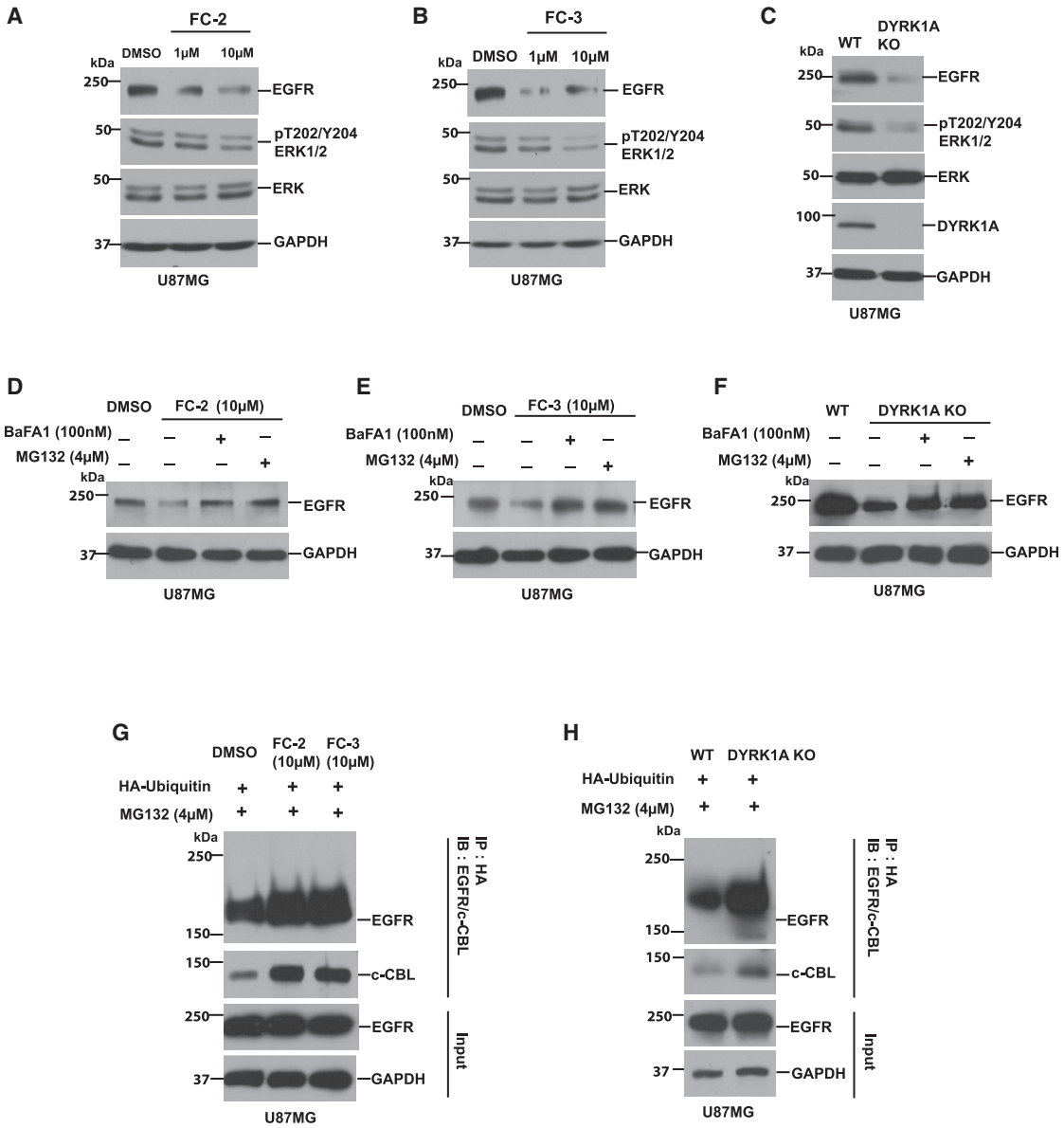

Figure 6. FC-2 and FC-3 destabilize EGFR in glioblastoma cell-based models

(A–C) Treatments with (A) FC-2 and (B) FC-3 and (C) CRISPR-CAS9 knockout of DYRK1A downregulated the total EGFR and ERK phosphorylation in U87MG cells; GAPDH was used as a loading control.

(D–F) Treatments with (D) FC-2 and (E) FC-3 and (F) DYRK1A knockouts (KOs) treated with the proteasomal inhibitor MG132 (4 μM) or the lysosomal inhibitor BaFA1 (100 nM) resulted in the accumulation of total EGFR; GAPDH was used as a loading control.

(G and H) Co-immunoprecipitation of HA-ubiquitin tagged U87MG tagged with HA-treated with MG132 results in pull-down of EGFR and c-CBL after. Treatment with (G) FC-2 or FC-3 and (H) KO of DYRK1A; GAPDH was used as a loading control. The immunoblots were done as three independent biological replicates.

mechanism of action of FC-2 and FC-3 against DYRK1A in subcutaneous xenograft models is the downregulation of EGFR.

When U87MG cell lines stably expressing luciferase were stereotactically injected into the brains of Nu/J nude mice, we observed that the tumors were notably smaller in the FC-2-treatment cohort than in the vehicle cohorts (Figures 7F and 7G). Additionally, the animals from the treatment cohort showed prolonged survival of 10 days compared with the vehicle group, indicating that FC-2 could cross the blood-brain barrier (BBB) and suppress tumor cell proliferation (Figure 7H). Similar results were observed in the case of the U87MG DYRK1A-knockout (KO) cell lines where the tumors formed in the knockout cohort were markedly smaller than those in the wild-type (WT) cohort (Figures 7I and 7J). These results were validated further by comparing the Ki67-stained brain sections of the wild-type and the knockout cohorts (Figure 7K). Collectively, these data show

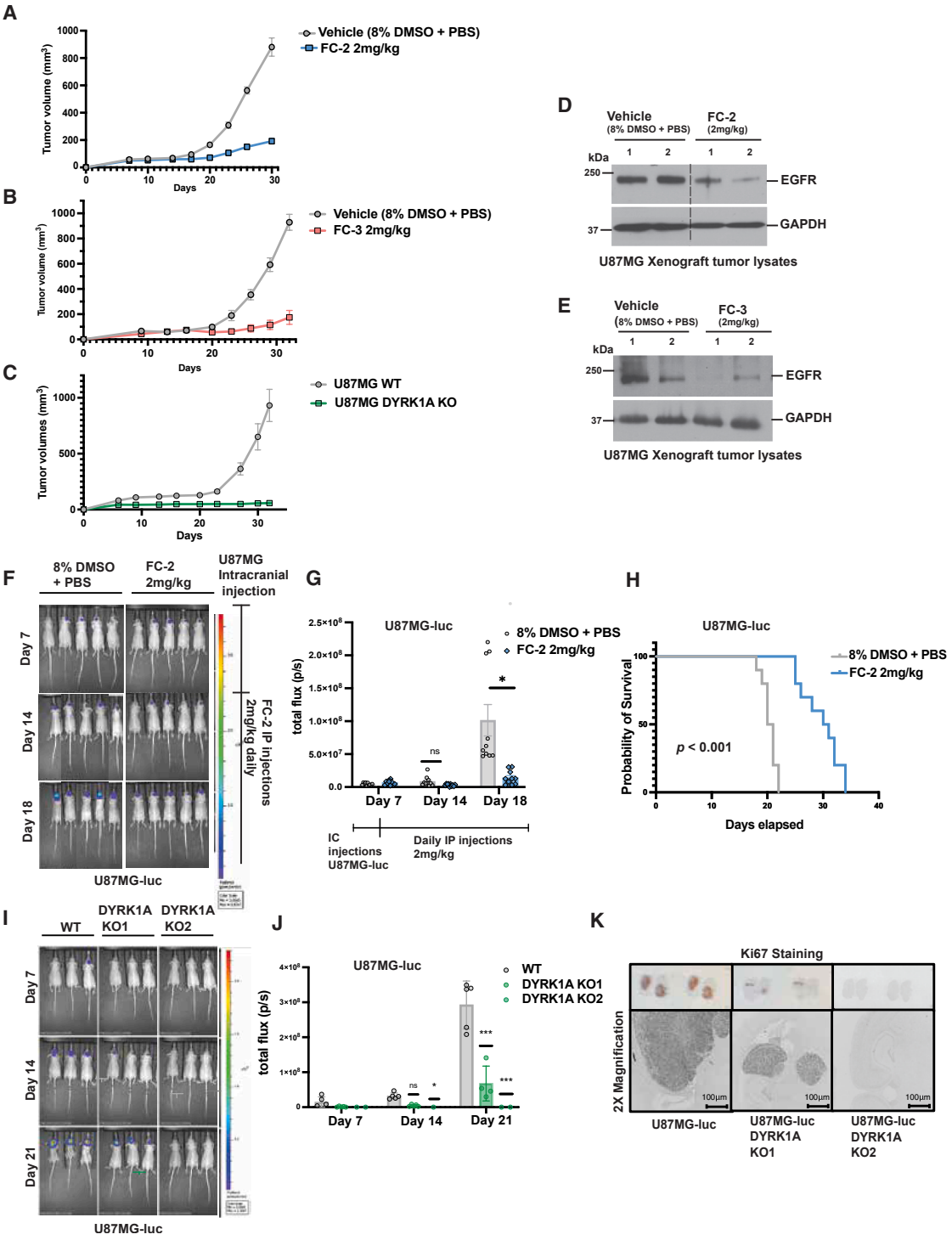

Figure 7. FC-2 and FC-3 attenuate DYRK1A-mediated tumorigenesis in GBM animal models

(A and B) Quantification of tumor volumes in a U87MG subcutaneous xenograft model of Nu/J nude mice (n = 6) treated with either vehicle (gray; 8% DMSO + PBS), FC-2 (blue; 2mg/kg daily), or FC-3 (red; 2mg/kg daily) over a period of 30 days.

(C) Quantification of tumor volumes in a U87MG subcutaneous xenograft model of Nu/J nude mice (n = 6) injected with wild-type (WT; gray) and DYRK1A-knockout (KO; green) cells on either flank over a period of 30 days.

(D and E) Western blot quantification of the total EGFR levels in the tumor lysates of two representative mice in the vehicle (8% DMSO + PBS) and FC-2 or FC-3 (2 mg/kg) treatment cohorts.

(F) Representative images of Nu/J nude mice intracranially injected with U87MG-luc cells and treated with vehicle (8% DMSO + PBS) or FC-2 (2 mg/kg daily). The cohorts were monitored by bioluminescence imaging for 18 days post-intracranial injection.

(legend continued on next page)

that FC-2 and FC-3 are reversible, small-molecule inhibitors capable of crossing the BBB (Figures S7A and S7B), reducing tumor burden, and prolonging survival in Nu/J intracranial as well as subcutaneous xenograft models.

DISCUSSION

DYRK1A is a multifunctional kinase that regulates diverse biological processes, including cell cycle progression, mRNA splicing, signal transduction, and neuronal development. Its dysregulation has been implicated in multiple pathological contexts, ranging from neurodevelopmental disorders such as Down syndrome to neurodegenerative diseases including Alzheimer disease, as well as various cancers.[54–58] In cancer models, several studies have implicated DYRK1A in oncogenic pathways, including EGFR stabilization,[17] resistance to apoptosis,[59] promotion of angiogenesis,[60] and evasion of stress responses.[61] Pharmacological inhibition of DYRK1A has been shown to block tumor formation in preclinical models of colon cancer and triple-negative breast cancer due to decreased expression of G2/M cell cycle regulators.[62] DYRK1A is also a potential therapeutic target in HNSCC, and its inhibition has been demonstrated to reduce invasion, colony formation, and tumor burden.[15] In non-small cell lung cancer (NSCLC), repression of DYRK1A by harmine was shown to enhance the sensitivity of EGFR-wild-type NSCLC cells to the EGFR inhibitor AZD9291 by regulating the STAT3-EGFR-Met signaling axis.[13] Another report identified that DYRK1A acts as a crucial contributor to tumor growth in PDAC by stabilizing the receptor protein tyrosine kinase c-Met receptor through the phosphorylation of SPRY2.[16] Furthermore, DYRK1A has been shown to promote epithelial-to-mesenchymal transition in hepatocellular carcinomas (HCCs).[63] The oncogenic signaling functions of DYRK1A across cancers highlight its potential as a therapeutic target. This is especially relevant in GBM where aberrant EGFR signaling, regulated by DYRK1A, is a key driver of tumor progression.[17]

GBM, a grade 4 glioma, is an aggressive primary brain tumor resistant to chemotherapy and radiotherapy. DYRK1A has been implicated in GBM tumorigenesis as it potentiates EGFR signaling by preventing the endocytic degradation of the receptor.[17,18] The current standard of care for GBM includes surgical resection followed by temozolomide administration, either concurrently or after radiotherapy[64,65]; however, most deaths occur within 2 years of diagnosis as these treatments are primarily palliative. Approximately 60% of primary aggressive GBM tumors are associated with EGFR upregulation.[66,67] DYRK1A plays an oncogenic role in GBM by modulating EGFR lysosomal targeting and self-renewal by phosphorylating SPRY2 at Thr75.[17,18] SPRY2, a modulator of the MAP kinase family, could act as an oncogene in certain subsets of GBM associated with EGFR amplification.[68] Thus, targeting DYRK1A in GBM may disrupt SPRY2 phosphorylation, thereby enabling enhanced endocytic degradation of EGFR and attenuating EGFR-driven oncogenic pathways. Due to its role in GBM, the kinase DYRK1A can be an attractive target for developing drug candidates against EGFR-dependent GBM.

Although small-molecule kinase inhibitors hold promise as drug candidates, selectivity issues often arise from the high degree of structural conservation across kinase catalytic domains, particularly within the ATP-binding pocket.[40,69–71] Sequence- and structure-based comparisons of residues in this region can highlight key determinants for the rational design of DYRK inhibitors. Strategies to exploit sequence variability typically focus on features such as the identity of the gatekeeper residue, opportunities for covalent bonding with cysteine side chains,[72] hydrogen-bonding interactions,[48] hinge-loop flexibility, the residue at the DFG minus 1 position,[73] and the overall dimensions of the ATP-binding pocket.[74,75] In the case of DYRKs, the gatekeeper residue is a bulky phenylalanine, which restricts access to the hydrophobic pocket of the kinase. Because many kinase inhibitors including imatinib and sorafenib show strong preferences for kinases with smaller gatekeeper residues, their affinity for DYRKs is generally low.[76,77] This structural distinction, however, opens opportunities for structure-guided discovery of DYRK-selective inhibitors that exploit alternative binding modes. A bulky hydrophobic residue (phenylalanine) at the DFG minus 1 position is another conserved feature in DYRK kinases, which we identify as an opportunity to exploit in the design of highly selective inhibitors. In addition to selectivity, kinase inhibitors could cause unanticipated side effects due to off-target effects as well as complex signaling crosstalk leading to drug toxicity.[78] For example, the DYRK inhibitor harmine, which is also a reversible inhibitor of MAO, has been found to be associated with potential toxicity and risks, triggering side effects such as nausea, vomiting, tremors, and psychoactivity, particularly at high doses.[33] Thus, off-target effects can obscure the direct effects of DYRK1A inhibition, making it a challenge to understand specific molecular mechanisms that are responsible for the desired therapeutic outcome.

In our study, we identified and characterized two potent, reversible small-molecule inhibitors of DYRKs, FC-2 and FC-3. Both compounds demonstrated on-target inhibition of DYRK1A, as confirmed by drug-resistant gatekeeper mutants (F238L-M240R) that preserved kinase function but abrogated inhibitor sensitivity in *in vitro* and cell-based models. FC-2 markedly reduced tumor volume and prolonged survival in subcutaneous and intracranial xenograft models, demonstrating its ability to cross the BBB. Our findings establish that FC-2 and

(G) Quantification of bioluminescence in the vehicle and FC-2 (2 mg/kg) treatment cohorts in the intracranial orthotopic xenograft mouse models ($n = 6$).
(H) Kaplan-Meyer representation of survival comparing vehicle (gray; 8% DMSO + PBS) and FC-2 (blue; 2 mg/kg) treatment cohort in the intracranial orthotopic xenograft model in Nu/J nude mice ($n = 6$); the treatment cohort survived 10 days longer than the vehicle cohort, with a p value < 0.001.
(I) Representative images of Nu/J nude mice intracranially injected with U87MG-luc cells and U87MG-luc DYRK1A KO1 and KO2 cells. The cohorts were monitored by bioluminescence imaging for 21 days post-intracranial injection.
(J) Quantification of bioluminescence in the U87MG-luc WT (gray) and U87MG-luc DYRK1A-KO (green) cohorts ($n = 6$) in the intracranial orthotopic xenograft mouse models.
(K) Ki-67 staining of the brain slices of Nu/J mice ($n = 6$) intracranially injected with U87MG-luc or U87MG-luc DYRK1A-KO1 and -KO2 clones. Staining images in 2× magnification are shown in the bottom. Symbols and error bars represent the mean value ± SEM. Welch's t test (*$p < 0.05$; **$p < 0.005$; ***$p < 0.0005$).

FC-3 effectively target DYRK1A in U87MG cells. Looking ahead, FC-2 and FC-3 may provide broader therapeutic benefits given DYRK1A's role in multiple cancers and diseases. DYRK1A inhibition has been shown to sensitize EGFR wild-type NSCLC cells to the EGFR inhibitor osimertinib or AZD9291.[13] Likewise, DYRK1A inhibitors could be effective in combination with EGFR-targeted therapies, potentially overcoming resistance mechanisms in many EGFR-driven cancers.[13,64] Together, these findings highlight the potential of FC-2 and FC-3 as promising leads for the development of DYRK1A-targeted therapies in GBM and beyond.

Limitations of the study

The study provides compelling proof-of-principle that FC-2 and FC-3 are potent DYRK-directed inhibitors and that DYRK1A supports EGFR-dependent GBM phenotypes. Nevertheless, the following aspects could be developed further. The study focused on a limited number of established GBM cell lines and xenograft models. As a result, it remains unclear how broadly the findings apply across the molecular and clinical heterogeneities of GBM, particularly in patient-derived tumors. Although the data support a DYRK1A-SPRY2-EGFR signaling axis, the study does not fully establish whether this pathway is the dominant mechanism underlying all observed phenotypes. Given the broad biology of DYRK1A, additional downstream effectors or parallel pathways may also contribute. The kinase profiling and inhibitor-resistant mutant experiments are important strengths, but because these compounds are ATP-competitive DYRK inhibitors, broader off-target and subfamily effects cannot be fully excluded, especially in more complex biological settings. The *in vivo* results are promising, but the preclinical package describing brain penetration, target engagement, durability of pathway inhibition, toxicity, and therapeutic window will require further development to support translation. Identification of biomarkers to define responsive tumor subsets, and combination studies with current GBM therapies or EGFR-targeted agents, would also aid translation.

RESOURCE AVAILABILITY

Lead contact

Requests for further information, resources, and reagents should be directed to and will be fulfilled by the lead contact, Nicholas K. Tonks (tonks@cshl.edu).

Materials availability

FC-2 and FC-3 generated in this study are available from the lead contact with a completed material transfer agreement.

Data and code availability

- The atomic coordinates and structure factors for the DYRK1A-FC-3 complex have been deposited in the Protein Data Bank under accession code PDB: 9YKO.
- No custom code was generated in this study.
- Any additional information required to reanalyze the data reported in this paper is available from the lead contact upon request.

ACKNOWLEDGMENTS

This study utilized the Animal facility (Woodbury), Flow Cytometry, Histology and Organoid core Shared Resources of the Cold Spring Harbor Laboratory Cancer Center. We are grateful to Prof. Alea Mills, CSHL, and her lab members Dr. Sherine Sun and Caizhi Wu for their help with neurosphere assay protocols and setup. We also thank Dr. Scott Lyons, CSHL, for his help with animal imaging. N.K.T. is the Caryl Boies Professor of Cancer Research at Cold Spring Harbor Laboratory. Research in N.K.T.'s lab was supported by NIH grant R01CA53840, the CSHL Cancer Center Support Grant CA044508, a grant from CART (Coins for Alzheimer's Research Trust), the CSHL-Northwell Health Affiliation, and the Hansen Foundation. Research in L.V.A.'s lab was supported by Penny's Flight Foundation and NIH grant R01MH119819. L.J.-T. is an investigator of the Howard Hughes Medical Institute.

AUTHOR CONTRIBUTIONS

P.V., L.V.A., D.P., L.J.-T., and N.K.T. designed research; P.V., E.E., A.G., K.F.C., A.A., M.H., K.T., E.M., C.G., and C.F. performed research; P.V., E.E., A.G., E.M., and C.G. analyzed data; P.V. and N.K.T. wrote the manuscript.

DECLARATION OF INTERESTS

N.K.T. is a member of the Scientific Advisory Board of DepYmed Inc. and Anavo Therapeutics. A patent application "Inhibitors of DYRK and PIM" US 2024/0199561 A1 was published on June 20, 2024.

STAR★METHODS

Detailed methods are provided in the online version of this paper and include the following:

- KEY RESOURCES TABLE
- EXPERIMENTAL MODEL AND STUDY PARTICIPANT DETAILS
  - Microbe strains
  - Cell lines
  - Animal models
- METHOD DETAILS
  - Preparation and characterization of benzothiazole derivatives
  - Reagents and plasmids
  - *In-vitro* ADP-Glo and peptide-based kinase assays
  - Protein expression and purification
  - Co-crystallization of DYRK1A-FC-3 and data collection
  - Generation of point mutants of DYRK1A and Sprouty2
  - Generation of CRISPR-CAS9 knockouts of DYRK1A, DYRK2 and DYRK3 and Sprouty2
  - Neurosphere assay
  - Invasion assay
  - Immunoblots
  - EGFR degradation and co-immunoprecipitation assays
  - Subcutaneous and intracranial xenografts
  - Immunohistochemistry
- QUANTIFICATION AND STATISTICAL ANALYSIS

SUPPLEMENTAL INFORMATION

Supplemental information can be found online at https://doi.org/10.1016/j.chembiol.2026.05.005.

Received: November 25, 2025
Revised: April 2, 2026
Accepted: May 13, 2026
Published: June 10, 2026

REFERENCES

1. Becker, W., and Sippl, W. (2011). Activation, regulation, and inhibition of DYRK1A. FEBS J. *278*, 246–256. https://doi.org/10.1111/j.1742-4658.2010.07956.x.
2. Soppa, U., and Becker, W. (2015). DYRK protein kinases. Curr. Biol. *25*, R488–R489. https://doi.org/10.1016/j.cub.2015.02.067.
3. Soundararajan, M., Roos, A.K., Savitsky, P., Filippakopoulos, P., Kettenbach, A.N., Olsen, J.V., Gerber, S.A., Eswaran, J., Knapp, S., and

Elkins, J.M. (2013). Structures of Down syndrome kinases, DYRKs, reveal mechanisms of kinase activation and substrate recognition. Struct. Lond. Engl. *21*, 986–996. https://doi.org/10.1016/j.str.2013.03.012.

4. Lee, P., Bhansali, R., Izraeli, S., Hijiya, N., and Crispino, J.D. (2016). The biology, pathogenesis and clinical aspects of acute lymphoblastic leukemia in children with Down syndrome. Leukemia *30*, 1816–1823. https://doi.org/10.1038/leu.2016.164.

5. Malinge, S., Bliss-Moreau, M., Kirsammer, G., Diebold, L., Chlon, T., Gurbuxani, S., and Crispino, J.D. (2012). Increased dosage of the chromosome 21 ortholog Dyrk1a promotes megakaryoblastic leukemia in a murine model of Down syndrome. J. Clin. Investig. *122*, 948–962. https://doi.org/10.1172/JCI60455.

6. Chaves, J.C.S., Machado, F.T., Almeida, M.F., Bacovsky, T.B., and Ferrari, M.F.R. (2020). microRNAs expression correlates with levels of APP, DYRK1A, hyperphosphorylated Tau and BDNF in the hippocampus of a mouse model for Down syndrome during ageing. Neurosci. Lett. *714*, 134541. https://doi.org/10.1016/j.neulet.2019.134541.

7. Ryoo, S.-R., Jeong, H.K., Radnaabazar, C., Yoo, J.-J., Cho, H.-J., Lee, H.-W., Kim, I.-S., Cheon, Y.-H., Ahn, Y.S., Chung, S.-H., and Song, W.J. (2007). DYRK1A-mediated hyperphosphorylation of Tau. A functional link between Down syndrome and Alzheimer disease. J. Biol. Chem. *282*, 34850–34857. https://doi.org/10.1074/jbc.M707358200.

8. Yin, X., Jin, N., Shi, J., Zhang, Y., Wu, Y., Gong, C.-X., Iqbal, K., and Liu, F. (2017). Dyrk1A overexpression leads to increase of 3R-tau expression and cognitive deficits in Ts65Dn Down syndrome mice. Sci. Rep. *7*, 619. https://doi.org/10.1038/s41598-017-00682-y.

9. Chu, D., Lei, L., Gu, S., Liu, F., and Wu, F. (2024). Dual-specificity tyrosine phosphorylation-regulated kinase 1A promotes the inclusion of amyloid precursor protein exon 7. Biochem. Pharmacol. *224*, 116233. https://doi.org/10.1016/j.bcp.2024.116233.

10. Abbassi, R., Johns, T.G., Kassiou, M., and Munoz, L. (2015). DYRK1A in neurodegeneration and cancer: Molecular basis and clinical implications. Pharmacol. Ther. *151*, 87–98. https://doi.org/10.1016/j.pharmthera.2015.03.004.

11. Kumar, K., Suebsuwong, C., Wang, P., Garcia-Ocana, A., Stewart, A.F., and DeVita, R.J. (2021). DYRK1A Inhibitors as Potential Therapeutics for β-Cell Regeneration for Diabetes. J. Med. Chem. *64*, 2901–2922. https://doi.org/10.1021/acs.jmedchem.0c02050.

12. Liu, H., Sun, Q., Chen, S., Chen, L., Jia, W., Zhao, J., and Sun, X. (2021). DYRK1A activates NFATC1 to increase glioblastoma migration. Cancer Med. *10*, 6416–6427. https://doi.org/10.1002/cam4.4159.

13. Li, Y.-L., Ding, K., Hu, X., Wu, L.-W., Zhou, D.-M., Rao, M.-J., Lin, N.-M., and Zhang, C. (2019). DYRK1A inhibition suppresses STAT3/EGFR/Met signalling and sensitizes EGFR wild-type NSCLC cells to AZD9291. J. Cell Mol. Med. *23*, 7427–7437. https://doi.org/10.1111/jcmm.14609.

14. Li, Y., Zhou, D., Xu, S., Rao, M., Zhang, Z., Wu, L., Zhang, C., and Lin, N. (2020). DYRK1A suppression restrains Mcl-1 expression and sensitizes NSCLC cells to Bcl-2 inhibitors. Cancer Biol. Med. *17*, 387–400. https://doi.org/10.20892/j.issn.2095-3941.2019.0380.

15. Radhakrishnan, A., Nanjappa, V., Raja, R., Sathe, G., Puttamallesh, V.N., Jain, A.P., Pinto, S.M., Balaji, S.A., Chavan, S., Sahasrabuddhe, N.A., et al. (2016). A dual specificity kinase, DYRK1A, as a potential therapeutic target for head and neck squamous cell carcinoma. Sci. Rep. *6*, 36132. https://doi.org/10.1038/srep36132.

16. Luna, J., Boni, J., Cuatrecasas, M., Bofill-De Ros, X., Núñez-Manchón, E., Gironella, M., Vaquero, E.C., Arbones, M.L., de la Luna, S., and Fillat, C. (2019). DYRK1A modulates c-MET in pancreatic ductal adenocarcinoma to drive tumour growth. Gut *68*, 1465–1476. https://doi.org/10.1136/gutjnl-2018-316128.

17. Pozo, N., Zahonero, C., Fernández, P., Liñares, J.M., Ayuso, A., Hagiwara, M., Pérez, A., Ricoy, J.R., Hernández-Laín, A., Sepúlveda, J.M., and Sánchez-Gómez, P. (2013). Inhibition of DYRK1A destabilizes EGFR and reduces EGFR-dependent glioblastoma growth. J. Clin. Investig. *123*, 2475–2487. https://doi.org/10.1172/JCI63623.

18. Zhang, P., Zhang, Z., Fu, Y., Zhang, Y., Washburn, M.P., Florens, L., Wu, M., Huang, C., Hou, Z., and Mohan, M. (2021). K63-linked ubiquitination of DYRK1A by TRAF2 alleviates Sprouty 2-mediated degradation of EGFR. Cell Death Dis. *12*, 608. https://doi.org/10.1038/s41419-021-03887-2.

19. Adayev, T., Wegiel, J., and Hwang, Y.-W. (2011). Harmine is an ATP-competitive inhibitor for dual-specificity tyrosine phosphorylation-regulated kinase 1A (Dyrk1A). Arch. Biochem. Biophys. *507*, 212–218. https://doi.org/10.1016/j.abb.2010.12.024.

20. De la Torre, R., De Sola, S., Pons, M., Duchon, A., de Lagran, M.M., Farré, M., Fitó, M., Benejam, B., Langohr, K., Rodriguez, J., et al. (2014). Epigallocatechin-3-gallate, a DYRK1A inhibitor, rescues cognitive deficits in Down syndrome mouse models and in humans. Mol. Nutr. Food Res. *58*, 278–288. https://doi.org/10.1002/mnfr.201300325.

21. Ogawa, Y., Nonaka, Y., Goto, T., Ohnishi, E., Hiramatsu, T., Kii, I., Yoshida, M., Ikura, T., Onogi, H., Shibuya, H., et al. (2010). Development of a novel selective inhibitor of the Down syndrome-related kinase Dyrk1A. Nat. Commun. *1*, 86. https://doi.org/10.1038/ncomms1090.

22. Rothweiler, U., Stensen, W., Brandsdal, B.O., Isaksson, J., Leeson, F.A., Engh, R.A., and Svendsen, J.S.M. (2016). Probing the ATP-Binding Pocket of Protein Kinase DYRK1A with Benzothiazole Fragment Molecules. J. Med. Chem. *59*, 9814–9824. https://doi.org/10.1021/acs.jmedchem.6b01086.

23. Rothweiler, U., Eriksson, J., Stensen, W., Leeson, F., Engh, R.A., and Svendsen, J.S. (2015). Luciferin and derivatives as a DYRK selective scaffold for the design of protein kinase inhibitors. Eur. J. Med. Chem. *94*, 140–148. https://doi.org/10.1016/j.ejmech.2015.02.035.

24. Stensen, W., Rothweiler, U., Engh, R.A., Stasko, M.R., Bederman, I., Costa, A.C.S., Fugelli, A., and Svendsen, J.S.M. (2021). Novel DYRK1A Inhibitor Rescues Learning and Memory Deficits in a Mouse Model of Down Syndrome. Pharmaceuticals *14*, 1170. https://doi.org/10.3390/ph14111170.

25. Salah, M., Abdel-Halim, M., and Engel, M. (2018). Design and synthesis of conformationally constraint Dyrk1A inhibitors by creating an intramolecular H-bond involving a benzothiazole core. Medchemcomm *9*, 1045–1053. https://doi.org/10.1039/C8MD00142A.

26. Aboushady, Y., Gabr, M., ElHady, A.K., Salah, M., Abadi, A.H., Wilms, G., Becker, W., Abdel-Halim, M., and Engel, M. (2021). Discovery of Hydroxybenzothiazole Urea Compounds as Multitargeted Agents Suppressing Major Cytotoxic Mechanisms in Neurodegenerative Diseases. ACS Chem. Neurosci. *12*, 4302–4318. https://doi.org/10.1021/acschemneuro.1c00475.

27. AlNajjar, Y.T., Gabr, M., ElHady, A.K., Salah, M., Wilms, G., Abadi, A.H., Becker, W., Abdel-Halim, M., and Engel, M. (2022). Discovery of novel 6-hydroxybenzothiazole urea derivatives as dual Dyrk1A/α-synuclein aggregation inhibitors with neuroprotective effects. Eur. J. Med. Chem. *227*, 113911. https://doi.org/10.1016/j.ejmech.2021.113911.

28. Meijer, L., Chrétien, E., and Ravel, D. (2024). Leucettinib-21, a DYRK1A Kinase Inhibitor as Clinical Drug Candidate for Alzheimer's Disease and Down Syndrome. J. Alzheimers Dis. JAD *101*, S95–S113. https://doi.org/10.3233/JAD-240078.

29. Lindberg, M.F., Deau, E., Miege, F., Greverie, M., Roche, D., George, N., George, P., Merlet, L., Gavard, J., Brugman, S.J.T., et al. (2023). Chemical, Biochemical, Cellular, and Physiological Characterization of Leucettinib-21, a Down Syndrome and Alzheimer's Disease Drug Candidate. J. Med. Chem. *66*, 15648–15670. https://doi.org/10.1021/acs.jmedchem.3c01888.

30. Liu, T., Wang, Y., Wang, J., Ren, C., Chen, H., and Zhang, J. (2022). DYRK1A inhibitors for disease therapy: Current status and perspectives. Eur. J. Med. Chem. *229*, 114062. https://doi.org/10.1016/j.ejmech.2021.114062.

31. Henderson, S.H., Sorrell, F., Bennett, J., Hanley, M.T., Robinson, S., Hopkins Navratilova, I., Elkins, J.M., and Ward, S.E. (2020). Mining Public Domain Data to Develop Selective DYRK1A Inhibitors. ACS Med. Chem. Lett. *11*, 1620–1626. https://doi.org/10.1021/acsmedchemlett.0c00279.

32. Ionescu, A., Dufrasne, F., Gelbcke, M., Jabin, I., Kiss, R., and Lamoral-Theys, D. (2012). DYRK1A kinase inhibitors with emphasis on cancer. Mini Rev. Med. Chem. *12*, 1315–1329. https://doi.org/10.2174/138955751120913 15.

33. Ables, J.L., Israel, L., Wood, O., Govindarajulu, U., Fremont, R.T., Banerjee, R., Liu, H., Cohen, J., Wang, P., Kumar, K., et al. (2024). A Phase 1 single ascending dose study of pure oral harmine in healthy volunteers. J. Psychopharmacol. *38*, 911–923. https://doi.org/10.1177/02698811241273772.

34. Bencze, G., Bencze, S., Rivera, K.D., Watson, J.D., Hidvegi, M., Orfi, L., Tonks, N.K., and Pappin, D.J. (2020). Mito-oncology agent: fermented extract suppresses the Warburg effect, restores oxidative mitochondrial activity, and inhibits in vivo tumor growth. Sci. Rep. *10*, 14174. https://doi.org/10.1038/s41598-020-71118-3.

35. Bencze, G., Venkataramani, P., Elkayam, E., Rivera, K.D., Garg, A., Szabadakai, I., Orfi, L., Joshua-Tor, L., Pappin, D.J., and Tonks, N.K. (2026). Identification and Validation of an Inhibitor of the Protein Kinases PIM and DYRK. J. Med. Chem. *69*, 7920–7932. acs.jmedchem.5c03226. https://doi.org/10.1021/acs.jmedchem.5c03226.

36. Zhang, X., Song, M., Kundu, J.K., Lee, M.-H., and Liu, Z.-Z. (2018). PIM Kinase as an Executional Target in Cancer. J. Cancer Prev. *23*, 109–116. https://doi.org/10.15430/JCP.2018.23.3.109.

37. Boni, J., Rubio-Perez, C., López-Bigas, N., Fillat, C., and de la Luna, S. (2020). The DYRK Family of Kinases in Cancer: Molecular Functions and Therapeutic Opportunities. Cancers *12*, 2106. https://doi.org/10.3390/cancers12082106.

38. Hastie, C.J., McLauchlan, H.J., and Cohen, P. (2006). Assay of protein kinases using radiolabeled ATP: a protocol. Nat. Protoc. *1*, 968–971. https://doi.org/10.1038/nprot.2006.149.

39. Wynn, M.L., Ventura, A.C., Sepulchre, J.A., García, H.J., and Merajver, S.D. (2011). Kinase inhibitors can produce off-target effects and activate linked pathways by retroactivity. BMC Syst. Biol. *5*, 156. https://doi.org/10.1186/1752-0509-5-156.

40. Miyazawa, K. (2011). Encountering unpredicted off-target effects of pharmacological inhibitors. J. Biochem. (Tokyo) *150*, 1–3. https://doi.org/10.1093/jb/mvr053.

41. Lin, A., Giuliano, C.J., Palladino, A., John, K.M., Abramowicz, C., Yuan, M.L., Sausville, E.L., Lukow, D.A., Liu, L., Chait, A.R., et al. (2019). Off-target toxicity is a common mechanism of action of cancer drugs undergoing clinical trials. Sci. Transl. Med. *11*, eaaw8412. https://doi.org/10.1126/scitranslmed.aaw8412.

42. Emrick, M.A., Lee, T., Starkey, P.J., Mumby, M.C., Resing, K.A., and Ahn, N.G. (2006). The gatekeeper residue controls autoactivation of ERK2 via a pathway of intramolecular connectivity. Proc. Natl. Acad. Sci. *103*, 18101–18106. https://doi.org/10.1073/pnas.0608849103.

43. Treiber, D.K., and Shah, N.P. (2013). Ins and outs of kinase DFG motifs. Chem. Biol. *20*, 745–746. https://doi.org/10.1016/j.chembiol.2013.06.001.

44. Keyloun, K.R., Reid, M.C., Choi, R., Song, Y., Fox, A.M.W., Hillesland, H.K., Zhang, Z., Vidadala, R., Merritt, E.A., Lau, A.O.T., et al. (2014). The gatekeeper residue and beyond: homologous calcium-dependent protein kinases as drug development targets for veterinarian Apicomplexa parasites. Parasitology *141*, 1499–1509. https://doi.org/10.1017/S0031182014000857.

45. Zuccotto, F., Ardini, E., Casale, E., and Angiolini, M. (2010). Through the "Gatekeeper Door": Exploiting the Active Kinase Conformation. J. Med. Chem. *53*, 2681–2694. https://doi.org/10.1021/jm901443h.

46. Bridges, A.J. (2001). Chemical Inhibitors of Protein Kinases. Chem. Rev. *101*, 2541–2572. https://doi.org/10.1021/cr000250y.

47. Alaimo, P.J., Knight, Z.A., and Shokat, K.M. (2005). Targeting the gatekeeper residue in phosphoinositide 3-kinases. Bioorg. Med. Chem. *13*, 2825–2836. https://doi.org/10.1016/j.bmc.2005.02.021.

48. Specht, K.M., and Shokat, K.M. (2002). The emerging power of chemical genetics. Curr. Opin. Cell Biol. *14*, 155–159. https://doi.org/10.1016/S0955-0674(02)00317-4.

49. Ferron, S.R., Pozo, N., Laguna, A., Aranda, S., Porlan, E., Moreno, M., Fillat, C., de la Luna, S., Sánchez, P., Arbonés, M.L., and Fariñas, I. (2010). Regulated segregation of kinase Dyrk1A during asymmetric neural stem cell division is critical for EGFR-mediated biased signaling. Cell Stem Cell *7*, 367–379. https://doi.org/10.1016/j.stem.2010.06.021.

50. Zhang, J., and Li, L. (2005). BMP signaling and stem cell regulation. Dev. Biol. *284*, 1–11. https://doi.org/10.1016/j.ydbio.2005.05.009.

51. Aranda, S., Alvarez, M., Turró, S., Laguna, A., and de la Luna, S. (2008). Sprouty2-mediated inhibition of fibroblast growth factor signaling is modulated by the protein kinase DYRK1A. Mol. Cell Biol. *28*, 5899–5911. https://doi.org/10.1128/MCB.00394-08.

52. Walsh, A.M., Kapoor, G.S., Buonato, J.M., Mathew, L.K., Bi, Y., Davuluri, R.V., Martinez-Lage, M., Simon, M.C., O'Rourke, D.M., and Lazzara, M.J. (2015). Sprouty2 Drives Drug Resistance and Proliferation in Glioblastoma. Mol. Cancer Res. *13*, 1227–1237. https://doi.org/10.1158/1541-7786.MCR-14-0183-T.

53. Park, J.-W., Wollmann, G., Urbiola, C., Fogli, B., Florio, T., Geley, S., and Klimaschewski, L. (2018). Sprouty2 enhances the tumorigenic potential of glioblastoma cells. Neuro Oncol. *20*, 1044–1054. https://doi.org/10.1093/neuonc/noy028.

54. Aranda, S., Laguna, A., and de la Luna, S. (2011). DYRK family of protein kinases: evolutionary relationships, biochemical properties, and functional roles. FASEB J. Off. Publ. Fed. Am. Soc. Exp. Biol. *25*, 449–462. https://doi.org/10.1096/fj.10-165837.

55. Demuro, S., Di Martino, R.M.C., Ortega, J.A., and Cavalli, A. (2021). GSK-3β, FYN, and DYRK1A: Master Regulators in Neurodegenerative Pathways. Int. J. Mol. Sci. *22*, 9098. https://doi.org/10.3390/ijms22169098.

56. Soppa, U., Schumacher, J., Florencio Ortiz, V., Pasqualon, T., Tejedor, F.J., and Becker, W. (2014). The Down syndrome-related protein kinase DYRK1A phosphorylates p27(Kip1) and Cyclin D1 and induces cell cycle exit and neuronal differentiation. Cell Cycle Georget. Tex *13*, 2084–2100. https://doi.org/10.4161/cc.29104.

57. Tejedor, F.J., and Hämmerle, B. (2011). MNB/DYRK1A as a multiple regulator of neuronal development. FEBS J. *278*, 223–235. https://doi.org/10.1111/j.1742-4658.2010.07954.x.

58. Thompson, B.J., Bhansali, R., Diebold, L., Cook, D.E., Stolzenburg, L., Casagrande, A.-S., Besson, T., Leblond, B., Désiré, L., Malinge, S., and Crispino, J.D. (2015). DYRK1A controls the transition from proliferation to quiescence during lymphoid development by destabilizing Cyclin D3. J. Exp. Med. *212*, 953–970. https://doi.org/10.1084/jem.20150002.

59. Laham, A.J., Saber-Ayad, M., and El-Awady, R. (2021). DYRK1A: a down syndrome-related dual protein kinase with a versatile role in tumorigenesis. Cell. Mol. Life Sci. *78*, 603–619. https://doi.org/10.1007/s00018-020-03626-4.

60. Rozen, E.J., Roewenstrunk, J., Barallobre, M.J., Di Vona, C., Jung, C., Figueiredo, A.F., Luna, J., Fillat, C., Arbonés, M.L., Graupera, M., et al. (2018). DYRK1A Kinase Positively Regulates Angiogenic Responses in Endothelial Cells. Cell Rep. *23*, 1867–1878. https://doi.org/10.1016/j.celrep.2018.04.008.

61. Guo, X., Williams, J.G., Schug, T.T., and Li, X. (2010). DYRK1A and DYRK3 Promote Cell Survival through Phosphorylation and Activation of SIRT1. J. Biol. Chem. *285*, 13223–13232. https://doi.org/10.1074/jbc.M110.102574.

62. Laham, A.J., El-Awady, R., Saber-Ayad, M., Wang, N., Yan, G., Boudreault, J., Ali, S., and Lebrun, J.-J. (2024). Targeting the DYRK1A kinase prevents cancer progression and metastasis and promotes cancer cells response to G1/S targeting chemotherapy drugs. npj Precis. Oncol. *8*, 128. https://doi.org/10.1038/s41698-024-00614-w.

63. Li, Y.L., Zhang, M.M., Wu, L.W., Liu, Y.H., Zhang, Z.Y., Zeng, L.H., Lin, N.M., and Zhang, C. (2022). DYRK1A reinforces epithelial-mesenchymal transition and metastasis of hepatocellular carcinoma via cooperatively

activating STAT3 and SMAD. J. Biomed. Sci. *29*, 34. https://doi.org/10.1186/s12929-022-00817-y.

64. Oprita, A., Baloi, S.-C., Staicu, G.-A., Alexandru, O., Tache, D.E., Danoiu, S., Micu, E.S., and Sevastre, A.-S. (2021). Updated Insights on EGFR Signaling Pathways in Glioma. Int. J. Mol. Sci. *22*, 587. https://doi.org/10.3390/ijms22020587.
65. Wirsching, H.-G., Galanis, E., and Weller, M. (2016). Glioblastoma. Handb. Clin. Neurol. *134*, 381–397. https://doi.org/10.1016/B978-0-12-802997-8.00023-2.
66. Xu, H., Zong, H., Ma, C., Ming, X., Shang, M., Li, K., He, X., Du, H., and Cao, L. (2017). Epidermal growth factor receptor in glioblastoma. Oncol. Lett. *14*, 512–516. https://doi.org/10.3892/ol.2017.6221.
67. Shergalis, A., Bankhead, A., Luesakul, U., Muangsin, N., and Neamati, N. (2018). Current Challenges and Opportunities in Treating Glioblastoma. Pharmacol. Rev. *70*, 412–445. https://doi.org/10.1124/pr.117.014944.
68. Ivliev, A.E., 'T Hoen, P.A.C., and Sergeeva, M.G. (2010). Coexpression Network Analysis Identifies Transcriptional Modules Related to Proastrocytic Differentiation and Sprouty Signaling in Glioma. Cancer Res. *70*, 10060–10070. https://doi.org/10.1158/0008-5472.CAN-10-2465.
69. Liao, J.J.-L. (2007). Molecular recognition of protein kinase binding pockets for design of potent and selective kinase inhibitors. J. Med. Chem. *50*, 409–424. https://doi.org/10.1021/jm0608107.
70. Weber, C., Sipos, M., Paczal, A., Balint, B., Kun, V., Foloppe, N., Dokurno, P., Massey, A.J., Walmsley, D.L., Hubbard, R.E., et al. (2021). Structure-Guided Discovery of Potent and Selective DYRK1A Inhibitors. J. Med. Chem. *64*, 6745–6764. https://doi.org/10.1021/acs.jmedchem.1c00023.
71. Huang, D., Zhou, T., Lafleur, K., Nevado, C., and Caflisch, A. (2010). Kinase selectivity potential for inhibitors targeting the ATP binding site: a network analysis. Bioinforma. Oxf. Engl. *26*, 198–204. https://doi.org/10.1093/bioinformatics/btp650.
72. Cohen, F.E., Pan, K.-M., Huang, Z., Baldwin, M., Fletterick, R.J., and Prusiner, S.B. (1994). Structural Clues to Prion Replication. Science *264*, 530–531. https://doi.org/10.1126/science.7909169.
73. Schröder, M., Bullock, A.N., Fedorov, O., Bracher, F., Chaikuad, A., and Knapp, S. (2020). DFG-1 Residue Controls Inhibitor Binding Mode and Affinity, Providing a Basis for Rational Design of Kinase Inhibitor Selectivity. J. Med. Chem. *63*, 10224–10234. https://doi.org/10.1021/acs.jmedchem.0c00898.
74. Traxler, P., and Furet, P. (1999). Strategies toward the Design of Novel and Selective Protein Tyrosine Kinase Inhibitors. Pharmacol. Ther. *82*, 195–206. https://doi.org/10.1016/S0163-7258(98)00044-8.
75. Liu, Y., Bishop, A., Witucki, L., Kraybill, B., Shimizu, E., Tsien, J., Ubersax, J., Blethrow, J., Morgan, D.O., and Shokat, K.M. (1999). Structural basis for selective inhibition of Src family kinases by PP1. Chem. Biol. *6*, 671–678. https://doi.org/10.1016/S1074-5521(99)80118-5.
76. Ung, P.M.-U., and Schlessinger, A. (2015). DFGmodel: Predicting Protein Kinase Structures in Inactive States for Structure-Based Discovery of Type-II Inhibitors. ACS Chem. Biol. *10*, 269–278. https://doi.org/10.1021/cb500696t.
77. Zhao, Z., Wu, H., Wang, L., Liu, Y., Knapp, S., Liu, Q., and Gray, N.S. (2014). Exploration of Type II Binding Mode: A Privileged Approach for Kinase Inhibitor Focused Drug Discovery? ACS Chem. Biol. *9*, 1230–1241. https://doi.org/10.1021/cb500129t.
78. Klaeger, S., Heinzlmeir, S., Wilhelm, M., Polzer, H., Vick, B., Koenig, P.-A., Reinecke, M., Ruprecht, B., Petzoldt, S., Meng, C., et al. (2017). The target landscape of clinical kinase drugs. Science *358*, eaan4368. https://doi.org/10.1126/science.aan4368.
79. Li, J., Xiong, N., West, K.L., Leung, M., Ching, Y.P., Huang, J., Yuan, J., Yu, C.-H., Leung, J., and Huen, M. (2024). Nuclear F-actin assembly on damaged chromatin is regulated by DYRK1A and Spir1 phosphorylation. Nucleic Acids Res. *52*, 8897–8912. https://doi.org/10.1093/nar/gkae574.
80. Tarumoto, Y., Lu, B., Somerville, T.D.D., Huang, Y.-H., Milazzo, J.P., Wu, X.S., Klingbeil, O., El Demerdash, O., Shi, J., and Vakoc, C.R. (2018). LKB1, Salt-Inducible Kinases, and MEF2C Are Linked Dependencies in Acute Myeloid Leukemia. Mol. Cell *69*, 1017–1027.e6. https://doi.org/10.1016/j.molcel.2018.02.011.
81. Kamitani, T., Kito, K., Nguyen, H.P., and Yeh, E.T. (1997). Characterization of NEDD8, a developmentally down-regulated ubiquitin-like protein. J. Biol. Chem. *272*, 28557–28562. https://doi.org/10.1074/jbc.272.45.28557.
82. Schneider, C.A., Rasband, W.S., and Eliceiri, K.W. (2012). NIH Image to ImageJ: 25 years of image analysis. Nat. Methods *9*, 671–675. https://doi.org/10.1038/nmeth.2089.
83. Vonrhein, C., Flensburg, C., Keller, P., Sharff, A., Smart, O., Paciorek, W., Womack, T., and Bricogne, G. (2011). Data processing and analysis with the *autoPROC* toolbox. Acta Crystallogr. D Biol. Crystallogr. *67*, 293–302. https://doi.org/10.1107/S0907444911007773.
84. McCoy, A.J., Grosse-Kunstleve, R.W., Adams, P.D., Winn, M.D., Storoni, L.C., and Read, R.J. (2007). *Phaser* crystallographic software. J. Appl. Crystallogr. *40*, 658–674. https://doi.org/10.1107/S0021889807021206.
85. Adams, P.D., Afonine, P.V., Bunkóczi, G., Chen, V.B., Davis, I.W., Echols, N., Headd, J.J., Hung, L.-W., Kapral, G.J., Grosse-Kunstleve, R.W., et al. (2010). *PHENIX* : a comprehensive Python-based system for macromolecular structure solution. Acta Crystallogr. D Biol. Crystallogr. *66*, 213–221. https://doi.org/10.1107/S0907444909052925.
86. Emsley, P., Lohkamp, B., Scott, W.G., and Cowtan, K. (2010). Features and development of *Coot*. Acta Crystallogr. D Biol. Crystallogr. *66*, 486–501. https://doi.org/10.1107/S0907444910007493.
87. Chen, V.B., Arendall, W.B., Headd, J.J., Keedy, D.A., Immormino, R.M., Kapral, G.J., Murray, L.W., Richardson, J.S., and Richardson, D.C. (2010). *MolProbity* : all-atom structure validation for macromolecular crystallography. Acta Crystallogr. D Biol. Crystallogr. *66*, 12–21. https://doi.org/10.1107/S0907444909042073.

STAR★METHODS

KEY RESOURCES TABLE

REAGENT or RESOURCE	SOURCE	IDENTIFIER
Antibodies		
DYRK1A	Santa Cruz	Cat# sc-100376; RRID: AB_1122375
EGFR	Santa Cruz	Cat# sc-373746; RRID: AB_10920395
GAPDH	Santa Cruz	Cat# sc-47724; RRID: AB_627678
pERK	Cell Signaling	Cat# 9101; RRID: AB_331646
ERK	Santa Cruz	Cat# sc-514302; RRID: AB_2571739
HA antibody	GenScript	Cat# A01621; RRID: AB_2622159
c-Cbl	Cell Signaling	Cat# 2747; RRID: AB_2275284
DYRK2	Santa Cruz	Cat# sc-293487
DYRK3	Santa Cruz	Cat# sc-390532
HRP goat anti-mouse	Abcam	Cat# ab6789; RRID: AB_955439
HRP goat anti-rabbit	Abcam	Cat# ab6721; RRID: AB_955447
Sprouty2	Santa Cruz	Cat# sc-518014
Bacterial and virus strains		
One Shot™ BL21(DE3) Chemically Competent E. coli	Thermo Fisher	Cat# C600003
Rosetta (DE3) Competent Cells - Novagen	Millipore Sigma	Cat# 70954-3
One Shot™ Stbl3™ Chemically Competent E. coli	Thermo Fisher	Cat# C737303
Chemicals, peptides, and recombinant proteins		
MG132	Sigma	Cat# M8699
Bafilomycin A1 (BaFA1)	Tocris Bioscience	Cat# 1334
B-27 Supplement minus Vitamin-A	Invitrogen	Cat# 12587010
Human EGF	Fujifilm Biosciences	Cat# 100-26
Human FGF-2	Fujifilm Biosciences	Cat# 100-28
Human PGDF-AA	Fujifilm Biosciences	Cat# 100-16
Human PGDF-BB	Fujifilm Biosciences	Cat# 100-18
Heparin	StemCell Technologies	Cat# 07980
Critical commercial assays		
ADP-Glo Kinase assay kit	Promega	Cat# V6930
Pierce™ BCA Protein Assay kit	Thermo Fisher	Cat# 23225
Quik Change II Site-directed Mutagenesis kit	Agilent technologies	Cat# 200523
Deposited data		
DYRK1A – FC-3 crystal structure	This paper	PDB ID: 9YKO https://www.rcsb.org/structure/9YKO
Experimental models: Cell lines		
Human: U87MG cells	ATCC	Cat# HTB-14
Human: LN229 cells	ATCC	Cat# CRL-2611

(*Continued on next page*)

Continued

REAGENT or RESOURCE	SOURCE	IDENTIFIER
Experimental models: Organisms/strains		
Mouse: Nu/J	The Jackson Laboratory	Strain #002019; RRID: IMSR_JAX:002019
Oligonucleotides		
Refer to Table S4 for all oligonucleotide sequences	This paper	N/A
Recombinant DNA		
pNIC28-Bsa4-DYRK1A	Gift from Nicola Burgess-Brown	Addgene; Cat# 38913
pET-28a-6xHis-Sumo-TEV-DYRK1A	This paper	N/A
pMH-SFB-DYRK1A	Li et al.[79]	Addgene; Cat# 101770
LentiV_Cas9_Puro	Tarumoto et al.[80]	Addgene; Cat# 108100
LRG2.1	Tarumoto et al.[80]	Addgene; Cat# 108098
HA-Ubiquitin	Kamitani et al.[81]	Addgene; Cat# 18712
pLuc	Gift from Scott Lyons, CSHL	N/A
pLV-mCherry/Neo-CMV>hSPRY2	VectorBuilder	This paper
pLV-mCherry/Neo-CMV>SPRY2T75 A	VectorBuilder	This paper
Software and algorithms		
ImageJ	Schneider et al.[82]	https://imagej.net/ij/
GraphPad Prism version 11.0	GraphPad Software, Boston, MA USA	www.graphpad.com
autoPROC	Vonrhein et al.[83]	https://www.globalphasing.com/autoproc/wiki/
PHASER	McCoy et al.[84]	https://phaser.io
PHENIX	Adams et al.[85]	https://phenix-online.org
COOT	Emsley et al.[86]	https://www2.mrc-lmb.cam.ac.uk/personal/pemsley/coot/
Molprobity	Chen et al.[87]	https://bio.tools/molprobity

EXPERIMENTAL MODEL AND STUDY PARTICIPANT DETAILS

Microbe strains

All microbial strains used in this study are listed in the key resources table. Bacterial strains were propagated according to standard laboratory procedures. Chemically competent *E. coli* Stbl3 cells were used for CRISPR-CAS9 cloning, and BL21(DE3) and Rosetta (DE3)-derived strains were used for recombinant protein expression for biochemical assays and crystallography studies, respectively. Cultures were grown in LB medium at 37°C with shaking unless otherwise noted. When required, antibiotics were added at the following final concentrations: ampicillin (100 μg/mL) and kanamycin (50 μg/mL). Strain identity was confirmed by sequencing analysis.

Cell lines

The cell lines U87MG (ATCC-HTB-14, human, male) and LN229 (ATCC-CRL-2611, human, female) were obtained from ATCC and cultured at 37°C with 5% CO2 using DMEM (Gibco) supplemented with 10% fetal bovine serum, GlutaMAX, and penicillin–streptomycin. Cells were confirmed to be mycoplasma-free using a mycoplasma detection kit (Lonza, Cat# LT07–218). Cell line authentication was performed for all cells using short tandem repeat (STR) testing.

Animal models

Six-week-old Nu/J nude female mice, sourced from The Jackson Laboratory (Strain #002019), were used for both subcutaneous and intracranial xenograft experiments with 6 animals per group. All animal experiments were conducted in accordance with NIH guidelines and were reviewed and approved by the Cold Spring Harbor Laboratory IACUC. Mice were housed five per cage (369 × 156 × 132 mm; 1145T, Tecniplast, UK) under controlled environmental conditions (12-h light/dark cycle; 20–25°C; 70–80% relative humidity), with food and water provided *ad libitum*.

METHOD DETAILS

Preparation and characterization of benzothiazole derivatives

Chemicals were obtained from commercial suppliers and used without further purification unless otherwise indicated. All ^{1}H NMR spectra were recorded on a Bruker Avance 300, 400 or 600 MHz. The ^{13}C NMR spectra were recorded at 100 or 125 MHz. Chemical shifts are relative to the deuterated solvent peak and are in ppm. The coupling constants (*J*) are measured in Hz. The 1H signals are described as s (singlet), d (doublet), t (triplet), q (quartet), m (multiplet), or br s (broad singlet). Low-resolution mass spectrometry was carried out at the LTQ XL™ Linear Ion Trap mass spectrometry. HPLC was performed using Waters system combining a 1525 binary PUMP. The analytical column was a Phenomenex Kinetex 2.6µm EVO C18 100Å 150x4.6mm. Chromatography was performed at ambient temperature with a flow rate of 1mL/min with a linear gradient from Water (0.05% TFA): AcCN (0.05% TFA)[95:5] to Water (0.05% TFA): AcCN (0.05% TFA) [5:95] in 15min, monitored/detected UV at 254nM by Photodiode Array (PDA) Detector.

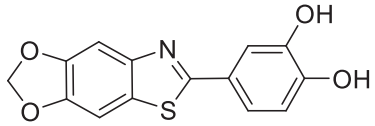

4-([1,3]dioxolo[4',5':4,5]benzo[1,2-d]thiazol-6-yl)benzene-1,2-diol (FC-2).

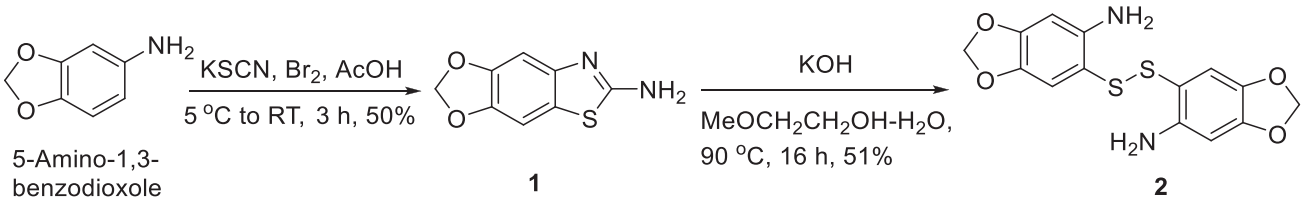

Synthesis of [1,3]Dioxolo[4',5':4,5]benzo[1,2-d]thiazol-6-amine (1)

To a stirred solution of 5-Amino-1,3-benzodioxole (3 g, 1 eq), KSCN (8.5 g, 4 eq) in acetic acid (22 mL) at 0°C, bromine (3.5 g, 1 eq) in acetic acid (22 mL) was added drop wise at 0 to 5°C over a period of 30 min. Reaction was allowed to room temperature and further stirred for 2 h. Reaction progress monitored by TLC analysis indicates complete consumption of starting material. Reaction mixture was diluted with water (100 mL) and basified with aqueous ammonia solution (50 mL), stirred for 30 min. The solid obtained was filtered and washed with water (1 x 20 mL) to get crude solid compound. Crude compound was purified by column chromatography (230-400 mesh silica gel, eluent 2% methanol in DCM) to afford [1,3]dioxolo[4',5':4,5]benzo[1,2-d]thiazol-6-amine (**1**) as pale green solid; yield 2.1 g (50%); ^{1}H NMR (DMSO-d6, 300 MHz) δ 7.251 (s, 1H), 7.192 (s, 2H), 6.924 (s, 1H), 5.958 (s, 2H).

Synthesis of 6,6'-Disulfanediylbis(benzo[d][1,3]dioxol-5-amine) (2)

To a stirred solution KOH (9 g) in water (9 mL) at room temperature, stirred for 10 minutes. Slowly added compound **1** (1.5 g, 1 eq) and 2-methoxyethanol (9 mL) at room temperature. Reaction heated to 90°C and stirred for 16 h. Reaction progress monitored by TLC analysis indicates complete consumption of starting material. Reaction mixture was cooled to 0°C, neutralized with acetic acid (15 mL) and stirred for 30 minutes. Extracted with ethyl acetate (2 x 150 mL), washed with water (1 x 25mL). Organic layer dried over anhydrous Na_2SO_4, filtered and evaporated under reduced pressure to obtain crude compound. Crude compound purified by column chromatography (230-400 mesh silica gel) eluted with 20% ethyl acetate in hexane to get 6,6'-disulfanediylbis(benzo[d][1,3]dioxol-5-amine) (**2**) as yellow solid; yield 700 mg (51%); ^{1}H NMR ($CDCl_3$, 300 MHz) δ 6.692 (s, 2H), 6.286 (s, 2H), 5.871 (s, 4H), 4.224 (br s, 4H).

Synthesis of FC-2 [4-([1,3]Dioxolo[4',5':4,5]benzo[1,2-d]thiazol-6-yl)benzene-1,2-diol]

To a solution of compound **2** (336 mg, 1 eq) in ethanol (15mL) was added sodium dithionate (700 mg, 4 eq) in water (5 mL) at room temperature followed by 3,4-dihydroxybenzaldehyde (280 mg, 2 eq) and the mixture was heated to reflux for 16 h. Reaction progress monitored by TLC analysis indicates complete consumption of starting material. Reaction mixture was cooled to room temperature and diluted with ethyl acetate (150 mL) and washed with water (1 x 50 mL). Organic layer was dried over anhydrous Na_2SO_4, filtered and evaporated under reduced pressure to afford crude compound. Crude compound was purified by column chromatography (230-400 mesh silica gel) eluted with 5% methanol in DCM to get 4 ([1,3]dioxolo[4',5':4,5]benzo[1,2-d]thiazol-6-yl)benzene-1,2-diol (**FC-2**)

and finally by prep HPLC as yellow solid; yield 280 mg (50%); ^{1}H NMR (DMSO-d6, 400 MHz) δ 9.435 (Br s, 2H), 7.598 (s, 1H), 7.488 (s, 1H), 7.442 (d, 1H, *J* = 2.16 Hz), 7.296 (dd, 1H, *J* = 2.16 & 8.2 Hz), 6.864 (d, 1H, *J* = 8.2 Hz), 6.128 (s, 2H); ^{13}C-NMR (DMSO-d6, 100 MHz) δ 100.864, 101.759, 101.908, 113.499, 116.080, 118.698, 124.669, 127.001, 145.745, 146.066, 147.566, 148.387, 148.652, 165.903; HPLC: RT = 8.326 min; purity 96.2% (254 nm). LRMS m/z calculated for $C_{14}H_9NO_4S$ [M+H] 288.03 found 288.17.

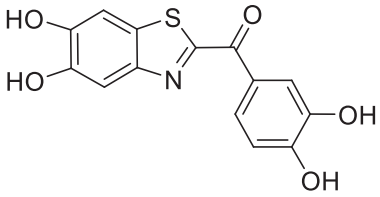

(5,6-dihydroxybenzo[d]thiazol-2-yl)(3,4-dihydroxyphenyl)methanone (FC-3).

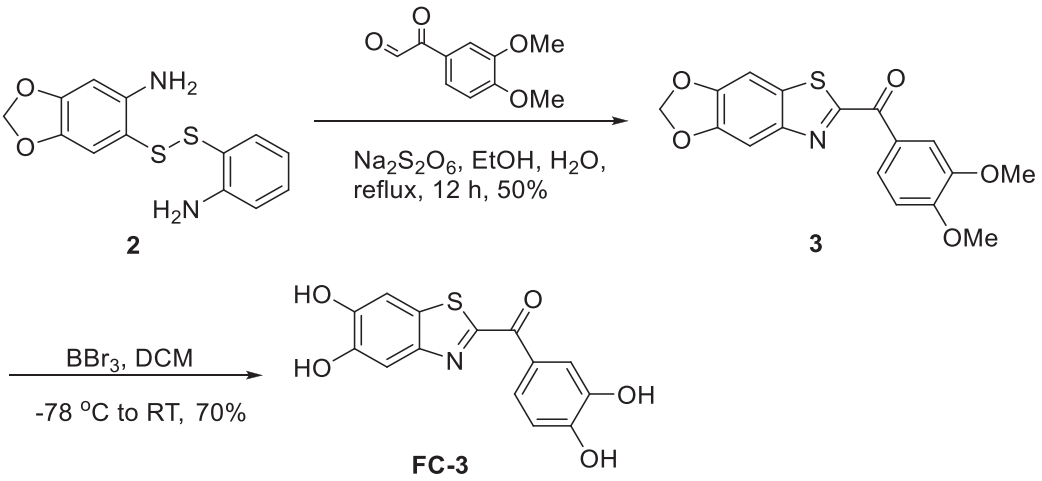

Synthesis of [1,3]dioxolo[4',5':4,5]benzo[1,2-d]thiazol-6-yl(3,4 dimethoxyphenyl)methanone (3)

To a solution of compound 2 (224 mg, 1 eq) in ethanol (15mL) was added sodium dithionate (466 mg, 4 eq) in water (5 mL) at room temperature followed by 2-(3,4-dimethoxyphenyl)-2-oxoacetaldehyde (260 mg, 2 eq) and heated to reflux for 12h. Reaction progress monitored by TLC analysis indicates complete consumption of starting material. Reaction mixture was cooled to room temperature and diluted with ethyl acetate (150 mL) and washed with water (1 x 50 mL). Organic layer was dried over anhydrous Na_2SO_4, filtered and evaporated under reduced pressure to afford crude compound. Crude compound was purified by column chromatography (230-400 mesh silica gel) eluted with 25% ethyl acetate in hexane to get [1,3]dioxolo[4',5':4,5]benzo[1,2-d]thiazol-6-yl(3,4-dimethoxyphenyl)methanone (**3**); yield 230mg (50%); ^{1}H NMR ($CDCl_3$, 300 MHz) δ 8.500 (dd, 1H, *J* = 2.1 & 8.7 Hz), 8.029 (d, 1H, *J* = 2.1 Hz), 7.556 (s, 1H), 7.337 (s, 1H), 7.009 (d, 1H, *J* = 8.4 Hz), 6.123 (s, 2H), 3.998 (s, 3H), 3.993 (s, 3H).

Synthesis of FC-3 [(5,6-Dihydroxybenzo[d]thiazol-2-yl)(3,4-dihydroxyphenyl)methanone]

To a stirred solution of compound **3** (180 mg, 1 eq) in DCM (10mL) at room temperature and cooled to -78°C in dry-ice-acetone bath. To this cooled solution was added BBr_3 (1M in DCM) (4.5mL, 8 eq) at -78°C and stirred for 30 min. Reaction mixture was allowed to room temperature and stirred for 16 h. Reaction progress monitored by TLC analysis indicates complete consumption of starting material. Reaction mixture was quenched with methanol at 0°C, stirred for 30 mins, reaction evaporated under reduced pressure to obtain crude compound. Crude compound was purified by prep HPLC to get 5,6-dihydroxybenzo[d]thiazol-2-yl)(3,4-dihydroxyphenyl)methanone (FC-3) as brown color solid; yield 111 mg (70%); ^{1}H NMR (DMSO-d6, 400 MHz) δ 8.074 (d, 1H, *J* = 8.4 Hz), 7.94 (d, 1H, *J* = 1.7 Hz), 7.511 (s, 1H), 7.445 (s, 1H), 6.932 (d, 1H, *J* = 8.4 Hz); ^{13}C-NMR (DMSO-d6, 100 MHz) δ 105.969, 108.972, 115.329, 117.662, 124.825, 126.285, 128.526, 145.165, 147.238, 147.599, 148.508, 151.883, 164.299, 181.947; HPLC: RT = 6.804 min; purity 94.7% (254 nm). LRMS m/z calculated for $C_{14}H_9NO_5S$ [M+H] 304.02 found 304.08. HPLC purity, 94.7% (254 nm).

Reagents and plasmids

FC-2 and FC-3 were resuspended in 100% DMSO to a stock concentration of 10mM and stored at -80°C. The oligonucleotides used in the study have been summarized in Table S4. The plasmid pNIC28-Bsa4-DYRK1A, a gift from Nicola Burgess-Brown (Addgene, Cat# 38913), for bacterial protein purification and pMH-SFB-DYRK1A[79] (Addgene, Cat# 101770) for mammalian expression were purchased from Addgene. Site-directed mutagenesis was done on these plasmids using the Quik Change II Site-directed Mutagenesis kit from Agilent Technologies (Cat #200523). The lentiviral vectors Cas9-puro and LRG2.1 were a gift from Chris Vakoc's lab, CSHL[80] (Addgene, Cat# 108100 and Cat# 108098). The plasmid pLuc-was a gift from Dr. Scott Lyons, CSHL. For the mammalian

expression of Sprouty2, the plasmids pLV-mCherry/Neo-CMV>hSPRY2 and pLV-mCherry/Neo-CMV>SPRY2T75A were designed and purchased from VectorBuilder, transiently transfected into U87MG Sprouty2 knockout cells using Lipofectamine 3000 transfection reagent (Thermofisher, Cat# L3000008) and used in neurosphere assays.

In-vitro ADP-Glo and peptide-based kinase assays

The 179 analogs of CSH-4044 were screened using the ADP-Glo Kinase assay kit from Promega (Cat# V6930). The screening was done using 384-well white assay plates (Corning). The radiometric peptide-based kinase assay was performed to validate the results and determine the IC50 of the inhibitors using the protocol described in.[38] The recombinant His-tagged (N-terminus) DYRK1A (127-485aa) and PIM1 kinases (313aa) were purified from bacterial BL21 (DE3) cells using Ni-NTA beads and assayed against the peptide sequences KKISGRLSPIMTEQ and RSRHSSYPAGT (gift from University of Dundee) for DYRK1A and PIM1 respectively at a final concentration of 10 μM in the assay buffer containing 25 mM HEPES, pH 6.8, 5 mM $MgCl_2$, 0.5 mM DTT and 1 mg/ml BSA. The [γ-^{32}P] ATP for the assay was purchased from Perkin Elmer (#BLU502A250UC). The specific activity of [γ-^{32}P] ATP was determined by dissolving and spiking non-radioactive 'cold' ATP (Sigma) in assay buffer using [γ-^{32}P] ATP to produce radioactivity of 1 x 10^5 to 1 x 10^6 c.p.m. per nmol. The kinase assay was performed either with or without inhibitors was performed at 30°C with a 10 mins incubation period. The reaction mixture (15μl) was then spotted onto 2x2 P81 phospho-cellulose papers (Whatman) that bind the peptide substrate. The excess ATP was then washed from the P81 papers with 75mM phosphoric acid using a wire mesh basket, three times followed by a final wash using acetone. The P81 papers were then dried and measured for radioactivity in a vial containing scintillating fluid using a scintillation counter (GMI Inc.). The data were then plotted using GraphPad Prism version 11.0 (GraphPad Software Inc., Boston, MA USA).

Protein expression and purification

For structural studies, the kinase domain of DYRK1A (aa 127-485) was cloned into a pET-28a expression vector with 6xHis-Sumo affinity tag followed by a TEV protease cleavage site. Expression and purification were done as previously described[3] with minor modifications. Briefly, pET-28a-6xHis-Sumo-TEV-DYRK1A was transformed into Rosetta 2 DE3 cells (Millipore Sigma #70954-3) and grown in LB media at 37°C, and protein expression was induced by adding 1 mM IPTG at 18°C for 16hrs at an OD ~0.6. After pelleting the cells by centrifugation (4000 rpm for 15 min) they were resuspended in 50 mM HEPES pH=7.5, 500 mM NaCl, 5% Glycerol, 5 mM Imidazole, 0.5 mM TCEP, and protease inhibitors cocktail. Cells were lysed by sonication, and insoluble pellets were removed by centrifugation at 20,000xg for 1hr. The cleared lysate was incubated with Ni-NTA beads for an hour, beads were washed with resuspension buffer, and the protein was eluted with the resuspension buffer supplemented with 250 mM Imidazole. TEV protease was then mixed into the protein and incubated at 4°C for 16hr to remove the 6xHis-sumo tag. Cleaved protein was loaded on a Mono S 5/50 column to remove the 6xHis-Sumo, DYRK1A was eluted with a 100-1000 mM NaCl linear gradient. DYRK1A was further purified by size exclusion chromatography using HiLoad 16/60 superdex 200 pg column pre-equilibrated with 20 mM HEPES pH=7.5, 500 mM NaCl, 5 mM DTT and 5 mM $MgCl_2$. Peak fractions were concentrated to 15 mg/ml, flashed frozen in LN_2 and stored at -80°C.

For cell-based assays, the 6xHis-tagged recombinant proteins DYRK1A, DYRK1A F238L, M240R, S242A and F238L-M240R were expressed from pMH-SFB-DYRK1A plasmid using BL21 (DE3) competent cells (Thermo Fisher, # C600003). Transformed cells were grown at 37°C to OD_{600} of 0.6 in Luria Bertani (LB) medium containing 50 μg/ml kanamycin and induced using 1mM isopropyl β-d-thiogalactopyranoside (IPTG, Gold Bio, #I2481C) at 16°C. After 16 hours, cells were harvested by centrifugation and resuspended in binding buffer [50 mM HEPES, 500 mM NaCl, 5 mM imidazole, 5% glycerol, Complete Mini protease inhibitor cocktail (Roche, #11836153001), PhosSTOP tablet (Roche/ PHOSS-RO, #4906845001), pH 7.5] and lysed using sonication. The cells were harvested by centrifugation, and the supernatants were filtered and incubated with Ni-NTA beads (Qiagen, #30210) that were pre-equilibrated with the binding buffer for 1 hour. The beads were then loaded onto the column and the flowthrough was collected. Then the column was washed sequentially using wash buffers - W1 (Binding buffer + 20 mM imidazole) and W2 (Binding buffer + 50 mM imidazole) buffers. The proteins were eluted from the column using a step-gradient of elution buffers containing increasing concentrations of imidazole (Binding buffer + 100-, 200-, and 300-mM imidazole) and were analyzed using SDS-PAGE. The fractions containing the desired protein were pooled with a purity > 95%, desalted using a PD-10 column (GE Healthcare, #17085101) and concentrated using an Amicon concentrator (10 kDa; Millipore Sigma, #UFC901008) at 4,000 rpm at 4°C. The protein concentrations were determined using Bradford assay and were aliquoted, flash-frozen in liquid nitrogen and stored at −80°C.

Co-crystallization of DYRK1A-FC-3 and data collection

Several attempts to crystallize the apo form of DYRK1A did not yield high-quality crystals. To promote crystallization, DYRK1A-FC-3 complex was formed by gradually adding 100 mM inhibitor to 10 mg/ml of DYRK1A until precipitation appeared at 1:1.1 molar ratio (DYRK1A: inhibitor). Precipitated protein and inhibitor were removed by centrifugation and the protein concentration determined to be at 7.5 mg/ml. Crystals were obtained by sitting-drop vapor diffusion method after mixing 0.1 mL of the protein-inhibitor complex at 7.5 mg/ml with 0.2 mL of 23% Glycerol, 16% PEG 8000 and 0.03 di-potassium hydrogen phosphate. Crystals appeared after 2 days and were fully grown after 5 days. Crystals were harvested and flash frozen into liquid nitrogen.

X-ray diffraction data were collected to 2.7 Å resolution at beamline 8.2.2 at the Berkeley Center for Structural Biology (BCSB) at the Advanced Light Source (ALS). Diffraction data were indexed, integrated, and scaled using autoPROC.[83] The phase problem was solved by molecular replacement with PHASER[84] using the DYRK1A structure excluding the small molecule as a search model

(PDB ID:3ANQ).[21] The molecular replacement solution was rigid body refined in PHENIX[85] followed by simulated annealing refinement prior to manual correction in COOT.[86] The final structure was refined to a R_{work}/R_{free} of 28/33% and validated using Molprobity.[87] X-ray data collection and refinement statistics for DYRK1A-FC-3 structure are summarized in Table S3. The atomic coordinates and structure factors for DYRK1A-FC-3 structure have been deposited in the Protein Data Bank under accession code 9YKO.

Generation of point mutants of DYRK1A and Sprouty2

Based on the crystal structure of DYRK1A with FC-3, a sequence alignment was done with DYRK and PIM kinases. Based on this, a few critical residues were selected that appeared to be important in DYRK1A-FC-3 binding. The plasmid pNIC28-Bsa4-DYRK1A was used to generate the point mutants F238L, M240R, S242A and F238L-M240R in the DYRK1A hinge region using The Quik Change II Site-directed Mutagenesis kit (Agilent Technologies #200523). For mammalian expression of the mutant proteins, all the above point mutants were generated in the plasmid pMH-SFB-DYRK1A and were transiently transfected into U87MG cells using Lipofectamine 3000 transfection reagent (Thermofisher, Catalog # L3000008) and was used in both neurosphere and invasion assays. For mammalian expression of Sprouty2, the plasmids pLV-mCherry/Neo-CMV>hSPRY2 and pLV-mCherry/Neo-CMV>SPRY2T75A were designed and purchased from VectorBuilder, transiently transfected into U87MG Sprouty2 knockout cells using Lipofectamine 3000 transfection reagent (Thermofisher, Catalog # L3000008) and used in neurosphere assays.

Generation of CRISPR-CAS9 knockouts of DYRK1A, DYRK2 and DYRK3 and Sprouty2

The CRISPR-CAS9 knockouts of DYRK1A, DYRK2, DYRK3 and Sprouty2 were generated using two guides targeting each kinase. The U87MG cells were stably transfected using the plasmid LentiV_Cas9_Puro [Addgene, 108100; generated using One Shot™ Stbl3™ Chemically Competent E. coli (Thermo Fisher, #C737303)] to stably express Cas9.The guide sequences used to generate DYRK1A, DYRK2, DYRK3 and Sprouty2 knockout clones have been summarized in Table S4. The guides were cloned into the plasmid LRG2.1 (Addgene, 108098). The plasmids were packaged into a lentivirus using the packaging plasmids VSVG and psPAX2 (Addgene, 12260). The plasmids were then stably transfected into U87MG and the cells were sorted for GFP using a single-cell sort into 96-well plates. The single cell clones were allowed to grow out and were screened using western blots for the presence of DYRK1A, DYRK2, DYRK3 or Sprouty2. The clones that were complete knockouts of DYRK1A, DYRK2, DYRK3 or Sprouty2 were selected for cell-based assays.

Neurosphere assay

The neurospheres were grown using U87MG cells in 6-well ultra-low-attachment plates (Corning #3471) in a serum-free medium containing 1X Tumor stem medium (TSM) base including Neurobasal-A Medium, DMEM/F-12 (1:1), HEPES buffer solution, 100mM MEM Sodium Pyruvate solution, 10mM MEM Non-essential amino acids solution, GlutaMAX-I supplement and Antibiotic-antimycotic solution (Invitrogen) supplemented with growth factors including B-27 Supplement minus Vitamin-A (Invitrogen, #12587010), Human-EGF (#100-26), Human-FGF-2 (#100-28), Human-PDGF-AA (#100-16), Human-PGDF-BB (#100-18) (Fujifilm Biosicences) and 0.2% Heparin (StemCell Technologies, # 07980). The growth factors were added just before seeding the cells to the TSM base medium. Working TSM was used within 24 hours of preparation. The neurospheres were seeded (5000 cells per well) and treated with increasing concentrations of inhibitors for a period of 72 hours. The inhibitors were then removed from the medium and the neurospheres were dissociated using TrypLE and re-seeded into 96-well low attachment plates at a low density of 500 cells per well in triplicates and monitored for 6 days for neurosphere growth. Images of the neurospheres were taken at 40X magnification and were analyzed for neurosphere diameter and numbers per well using ImageJ[82] and GraphPad Prism software version 11.0 ((GraphPad Software Inc., Boston, MA USA). For the CRISPR-CAS9 DYRK1A knockout experiments, the U87MG and LN299 DYRK1A knockout cell lines were seeded directly at a low density directly into 96-well low attachment plates and monitored for 6 days for neurosphere formation and compared to their wild-type counterparts.

Invasion assay

U87MG cells were either treated for 24 hours with vehicle, FC-2 or FC-3, followed by a drug-free wash prior to seeding. For trans-well invasion assays, 1 x 10^5 cells were seeded in the top chamber with Matrigel-coated membranes (Corning Cat. No. 354480, 24-well insert, pore size: 8 mm)., Cells in the upper chamber were seeded in serum-free DMEM, while media with 10% FBS was added to the lower chamber. The plates were incubated for 24 hours at 37°C, following which the cells on the upper surface were removed using cotton swabs. The membranes were then fixed in methanol and stained with crystal violet dye. The membranes were cut out and mounted on to slides. They were imaged at 40x (15-20 images) and counted to obtain the average number of cells per field that invaded. Two to three chambers were used per cell line and/or condition. For the CRISPR-CAS9 DYRK1A-knockout experiments, the U87MG DYRK1A-knockout cell lines were seeded directly at a low density directly into the upper chamber of the trans-well and incubated for 24hrs at 37°C. The membranes were then fixed, stained and analyzed for the number of invaded cells and compared to their wild-type counterparts.

Immunoblots

Whole cell lysates were harvested and resuspended in RIPA buffer [25 mM Tris, pH 7.4, 150 mM NaCl, 1% Triton X 100, 0.5% sodium deoxycholate, 0.1% sodium dodecyl sulfate, protease inhibitor cocktail (Sigma, Cat. No. 4693159001), and phosphatase inhibitor cocktail (Sigma, Cat. No. 4906845001)]. Quantification of protein concentration was done using the Pierce™ BCA Protein Assay

kit (ThermoFisher, Catalog #23225). Equal amounts of lysate were denatured and loaded onto a 10% SDS-PAGE gel. Antibody blocking was done with 5% milk in TBST (19 mM Tris base, NaCl 137 mM, KCl 2.7 mM and 0.1% Tween-20) for 1 hour at room temperature except for pERK p44/42 which used 5% BSA in TBST. The antibodies used for the western blots and co-immunoprecipitation studies are listed in STAR Methods. Blots were incubated with the primary antibody overnight at 4°C. Membranes were washed three times at room temperature (10 mins each) before they were incubated with secondary antibodies for one hour at room temperature. HRP goat anti-mouse (Bio-Rad; Cat. No. 1706516) at 1:50,000 was used for tubulin blots while HRP goat anti-rabbit (Abcam, Cat. No. ab6721) at 1:30,000 was used for all other primary antibodies. Membranes were washed 3 times again (15 min each) and developed using SuperSignal™ West Dura Extended Duration Substrate (ThermoFisher, Catalog #34075) and BioExcell autoradiographic film (Worldwide Medical, Catalog # 41101001). All the experiments were performed as three independent biological replicates.

EGFR degradation and co-immunoprecipitation assays

For the EGFR degradation assay, the U87MG wild-type cells were initially treated with DYRK inhibitors - 10μM FC-2 or FC-3. At the 20-hour timepoint, they were treated with the proteasomal inhibitor MG132 (Sigma, #M8699**)** at 4μM or the lysosomal inhibitor Bafilomycin A1 (BaFA1, Tocris, #1334) at 100nM for 4 hours, following which the cells were harvested and lysed for analysis by immunoblotting. Similarly, the U87MG DYRK1A KO clones were also treated with either 4μM MG132 or 100nM BaFA1 for 4 hours prior to lysate collection. For the co-immunoprecipitation assay, U87MG wild-type (WT) and U87MG-DYRK1A knockout (KO) clones were stably transfected with HA-Ubiquitin plasmid from Addgene[81] (Catalog #18712). The U87MG-WT stably expressing HA-ubiquitin were treated with either DMSO, FC-2 or FC-3 for 20 hrs then for 4hrs in the presence of 4μM MG132 before being harvested at 24hrs. After treatment, the cells were lysed using RIPA buffer and were pulled down using Pierce™ Anti-HA Magnetic Beads (ThermoFisher, Catalog #88836). The cells were then washed thrice using RIPA buffer using DynaMag™-2 Magnet rack (ThermoFisher, Catalog # 12321D). Elution from the beads was done by adding 50μl of 2 X SDS loading dye to 50μl of beads and heating the mixture for 10 mins at 50°C. The beads were then pelleted, and the supernatant was transferred to a new tube. The elution step was repeated twice, and the samples were pooled together. The samples were probed on immunoblots using antibodies against EGFR and c-CBL. All the experiments were performed as three independent biological replicates.

Subcutaneous and intracranial xenografts

For the subcutaneous xenografts, 1 x 10^6 U87MG or U87MG-DYRK1A KO cells were mixed with Matrigel and injected in the flanks of Nu/J nude mice (n=6 per cohort) (Jackson Laboratories). The tumors were allowed to grow to an average size of 100mm^3 after which daily intraperitoneal injections were started using either vehicle (8% DMSO in PBS) or 2mg/kg (in 8% DMSO in PBS) of FC-2 or FC-3. The tumor sizes were measured using a Vernier caliper and the mice weights were monitored regularly. The biological end point of the experiment was reached when the tumor size on the flanks exceeded 1 cm^3 or were ulcerated. Intracranial orthotopic injections were performed stereotactically by injecting 50,000 U87MG-luc (stably expressing luciferase) cells in Nu/J nude mice (n=6 per cohort) (Jackson laboratories) resuspended in 2μl of culture medium. The injections were administered in the bregma (coordinates: A-P, -1mm; M-L, 2mm; D-V, 3mm) using a Hamilton syringe. The animals were allowed to recover post-surgery and were monitored carefully. The mice brains were imaged using bioluminescent imaging by injecting luciferin (Gold Bio) intraperitoneally.

Immunohistochemistry

Mouse brain sections were analyzed using both H&E and Ki-67 staining after the orthotopic intracranial xenograft experimental end point. To obtain brain sections, the mice were anesthetized with isoflurane and were perfused trans-cardially using 4% paraformaldehyde [(PFA) Sigma Aldrich] dissolved in PBS. The mice brains were then post-fixed at 4°C using 4% PFA dissolved in PBS. The post-fixed brains were then cut into 10-μm coronal sections using a CM3050S cryostat (Leica Biosystems). The immunohistochemistry analysis of the mice brain slices was performed on the Discovery Ultra automatic IHC platform (Roche) following standard protocols by the CSHL Histology core. For the H&E staining, the slides were stained with hematoxylin (Hematoxylin 560 MX, Leica) for 30 seconds using the Leica Multistainer (ST5020) after being deparaffinized and rehydrated, followed by destaining in Define MX-aq (Leica) for 30 sec and bluing in Blue Buffer 8 (Leica) for 1min. After this step, the slides were stained with eosin (EOSIN 515 LT, Leica) for 30sec. This was followed by dehydration after which a robotic cover-slipper was used to add coverslips over the slides (Leica CV5030). For the Ki-67 staining, antigen retrieval (Benchmark Ultra CC1, Roche) was performed on the slides shortly after deparaffinization and rehydration at 96°C for 64 minutes. The slides were then incubated with Ki-67 antibody (Spring Bioscience, #M3062 – 1:500 dilution) at 37°C for 1hr. The immune signals were detected and amplified using the discovery multimer detection system (Discovery OmniMap HRP, Discovery DAB and Purple, Roche).

QUANTIFICATION AND STATISTICAL ANALYSIS

All *in vitro* experiments were performed with at least three independent biological replicates. *In vivo* experiments were conducted using female Nu/J nude mice, with 6 animals per group. Data are presented as mean ± SEM unless otherwise indicated in the figure legends. Statistical analyses were performed using GraphPad Prism (version 11.0), employing unpaired or multiple unpaired t tests as specified in the figure legends. Statistical significance was defined as $p < 0.05$ (*, $p < 0.05$; **, $p < 0.005$; ***, $p < 0.0005$). Additional details regarding statistical tests and sample sizes (n) are provided in the figure legends.